Revision 1, Nov. 3, 2013

Detection of Iron Substitution in Natroalunite-Natrojarosite Solid Solutions and Potential Implications for Mars

Thomas M. McCollom[1], Bethany L. Ehlmann[3,4], Alian Wang[5], Brian M. Hynek[1,2], Bruce Moskowitz[6,7], and Thelma S. Berquó[8]

[1]Laboratory for Atmospheric and Space Physics and [2]Department of Geological Sciences, University of Colorado, Boulder CO 80309, USA; [3]California Institute of Technology, Pasadena, CA, 91125; [4]Jet Propulsion Laboratory, California Institute of Technology, Pasadena, CA, 91109; [5]Deptartment of Earth and Planetary Sciences and McDonnell Center for Space Sciences, Washington University, St. Louis, MO, 63130; [6]Department of Earth Sciences and [7]Institute for Rock Magnetism, University of Minnesota, Minneapolis, MN 55455; [8]Department of Physics, Concordia College, Moorhead, MN 56562

Abstract – Natroalunite containing substantial amounts of Fe occurs as a prominent secondary phase during acid-sulfate alteration of pyroclastic basalts in volcanic fumaroles in Nicaragua and elsewhere, and has been observed in laboratory simulations of acid-sulfate alteration as well. Reaction path models constrained by field and experimental observations predict that Fe-rich natroalunite should also form as a major secondary phase during alteration of martian basalt under similar circumstances. Here, we evaluate the potential to use spectroscopic methods to identify minerals from the alunite group with compositions intermediate between natroalunite and natrojarosite on the surface of Mars, and to remotely infer their Fe contents. X-ray diffraction and spectroscopic measurements (Raman, visible/near infrared, mid-infrared, Mössbauer) were obtained for a suite of synthetic solid solutions with a range of Fe contents ranging from natroalunite to natrojarosite. In the visible/near infrared, minerals with intermediate compositions display several spectral features not evident in endmember spectra that could be used to remotely identify these minerals and infer their composition. In addition,

Raman spectra, mid-infrared spectra, and X-ray diffraction peaks all show systematic variation with changing Fe content, indicating that these methods could potentially be used to infer mineral compositions as well. The results suggest that alunite group minerals with intermediate Fe compositions may be able to account for some visible/near-infrared and Mössbauer spectral features from Mars that had previously been unidentified or attributed to other phases. Overall, our findings indicate that consideration of solid solutions may lead to new identifications of alunite group minerals on the surface of Mars, and raise the possibility that minerals with compositions intermediate between natroalunite and natrojarosite may be widely distributed on the planet.

Keywords: Mars, alunite group, visible/near infrared spectra, Raman spectra, hydrothermal, acid-sulfate alteration.

INTRODUCTION

Minerals in the alunite group have the ideal molecular formula $AB_3(SO_4)_2(OH)_6$, where the *A* site is most commonly occupied by the monovalent ions K^+, Na^+, and H_3O^+ (hydronium) and the *B* site is occupied primarily by Al^{3+} and Fe^{3+} (for convenience, we use here the term "alunite subgroup" to refer collectively to alunite and natroalunite, and "jarosite subgroup" to refer to jarosite, natrojarosite, and hydroniumjarosite; Table 1) (Stoffregen et al. 2000; Mills et al. 2009). In natural systems, minerals in the alunite and jarosite subgroups exhibit extensive solid solution mixing in the *A* site. In contrast, reports of mixing between Al and Fe on the *B* site among these minerals are more limited, with most published compositions having compositions close to either the Al or Fe endmembers (Dutrizac and Jambor 2000; Stoffregen et al. 2000; Papike et al. 2006, 2007). Reports of minerals in the alunite subgroup containing more than a few mole percent Fe in the *B* site have been particularly rare. In contrast, minerals with a full range of Fe-Al compositions intermediate between endmembers from the alunite and jarosite subgroups can be readily synthesized in the laboratory from mixtures of sulfate salts (Brophy et al. 1962; Härtig et al. 1984; McCollom et al. 2013a). More extensive solid solution mixing between Fe and Al in the *B* site has been reported for other minerals in the broader alunite supergroup, but these observations appear to be limited to those minerals where there is substantial (>55%) substitution of PO_4^{3-} or other trivalent anions in the sulfate site as well as >80% substitution of a divalent cation in the *A* site (e.g., Scott, 1987).

In recent studies, natroalunites containing substantial amounts of Fe were observed in acid-sulfate altered mineral deposits from fumaroles at Cerro Negro (CN) volcano and other volcanic sites in Nicaragua (Fig. 1) (McCollom et al. 2013b; Hynek et al. 2013). Precipitation of minerals

from the alunite group with a broad range of compositions intermediate between natroalunite and natrojarosite were also found to precipitate during incipient acid-sulfate alteration of basalt in laboratory experiments (McCollom et al. 2013a). In both cases, the Fe-rich natroalunites occur along with amorphous silica and Ca-sulfates (gypsum or anhydrite) as the predominant secondary phases formed during the initial stages of acid-sulfate alteration, together with minor hematite and other trace phases. The co-occurrence of Fe-bearing natroalunite with amorphous silica ± hematite during acid-sulfate alteration of basalt may be a common circumstance, since apparently similar assemblages have been reported in altered basaltic tephra from Hawaii (Morris et al. 2005; Bishop et al. 2007). In these cases, however, detailed chemical analyses of the natroalunite were not provided.

The Fe-rich natroalunites found at Cerro Negro precipitate from Fe, Al, and Na released by dissolution of primary igneous phenocrysts in the basalt (including plagioclase, olivine, and augite) as they react with sulfuric acid (McCollom et al. 2013b). The sulfuric acid in the fumaroles is produced during cooling and condensation of SO_2-bearing volcanic vapors through reactions such as:

$$3SO_2 + 2H_2O \rightarrow 2H_2SO_4 + S^0. \quad (1)$$

Natroalunite is absent from the most extensively altered deposits at Cerro Negro, suggesting that this mineral may form as a transient phase during the early stages of alteration, and then disappears as Na, Al, and Fe are mobilized from the deposits during more extensive alteration. In both the natural samples and experimental products, the close spatial association of the Fe-bearing natroalunite with amorphous silica and spheroidal hematite (Figs. 1, 2) suggests that these minerals precipitate concurrently. The apparent transient nature of the Fe-rich natroalunites in fumarole deposits together with the paucity of detailed chemical analyses of

alunite subgroup minerals found in such settings may account for the lack of previous literature reports of natroalunites with elevated Fe contents.

Reaction-path models based on constraints provided by field and laboratory observations predict that Fe-rich natroalunite should also occur as a major product during hydrothermal acid-sulfate alteration of pyroclastic basalts on Mars (McCollom et al. 2013a,b). The possibility that Fe-bearing natroalunites might be present on Mars, where they could potentially serve as indicators of incipient acid-sulfate alteration in fumarolic environments, led us to investigate methods by which they could be detected remotely. We report here on the spectral characteristics of solid solutions in this mineral group, focusing on the impact of Fe-Al solid solution mixing in the *B* site. While there have been a number of previous studies on the spectral properties of pure endmembers in the alunite and jarosite subgroups (e.g., Serna et al. 1986; Sasaki et al. 1998; Bishop and Murad 2005; Frost et al. 2006a,b; Murphy et al. 2009; Maubec et al. 2012), to our knowledge there are no previously published investigations of solid solutions with compositions intermediate between the endmembers. Accordingly, spectral measurements were made on synthetic solid solutions with compositions intermediate between natroalunite and natrojarosite, and are compared with field and laboratory spectra of natural samples containing Fe-bearing natroalunite.

METHODS

Synthetic mineral solid solutions with compositions intermediate between natroalunite and natrojarosite were produced from mixtures of Na-, Al-, and Fe-sulfate salts by heating the salts with 0.1 M H_2SO_4 at 145 °C for 2-6 days in Teflon-lined reaction vessels, as described in McCollom et al. (2013a). The chemical composition of the synthesized minerals was determined by dissolving an aliquot in a combination of concentrated HNO_3 and HCl, and analyzing the

resulting fluids by inductively coupled plasma – atomic emission spectroscopy (ICP-AES). Additional characterization of the morphology and chemical composition of synthetic and natural minerals were performed using a combination of scanning electron microscopy (SEM) equipped with an electron-dispersive X-Ray spectrometer (EDS), X-ray diffraction (XRD), and electron microprobe analysis (EMPA). X-ray diffraction analyses were performed with a Terra instrument (inXitu Incorporated, Campbell, CA) using Cu*K*α radiation, which is functionally equivalent to the ChemMin instrument deployed on the Curiosity rover on Mars (Blake et al. 2012). The SEM analyses were conducted on a JEOL 6480LV in backscattered electron (BSE) mode with an accelerating voltage of 15 kV. The EDS analyses were performed using an Oxford Instruments collector and processed using INCA software. Most analyses were performed on samples mounted on aluminum stubs using double-sided carbon tape and analyzed uncoated. In a few cases, samples were mounted in epoxy and polished in order to examine the minerals in cross-section. Electron microprobe analyses were performed using a JEOL JXA 8600 equipped with four wavelength-dispersive spectrometers. Samples were analyzed with an accelerating voltage of 15 kV, a 5 μm beam, and a beam current of 10 nA. Anhydrite was used as the standard for sulfur.

Laser Raman spectroscopic measurements of powdered synthetic natroalunite-natrojarosite solid solutions were made using a HoloLab5000-532 (Kaiser Optical System, Inc.). The instrument uses a 532 nm line from a frequency-doubled Nd:YVO_4 laser for excitation and a 20X, long-working-distance objective with numerical aperture (NA) of 0.4 for Raman signal collection, which produced a well-focused laser beam of ~6 μm diameter at the sampling spot. The system is functionally equivalent to the Mars Microbeam Raman Spectrometer (MMRS) under development for robotic planetary surface exploration (Wang et al. 2003). The

measurements cover a spectral range of 100-4000 cm^{-1} with a resolution of ~4-5 cm^{-1}. With a standard wavelength calibration procedure, the wavelength accuracy is <0.5 cm^{-1}, and precision is estimated to be <0.3 cm^{-1}. To check the chemical homogeneity of each sample, 5-10 Raman spectra were obtained from each powdered sample. Raman spectra for the endmembers of this series of synthetic solid solution were confirmed by comparison with standard spectra for natroalunite and natrojarosite. Because of their small size, Raman spectra of natural samples were recorded using a Horiba LabRAM HR confocal spectrometer with a 17 mW, 633 nm line of a HeNe laser as excitation source. Individual spectra were recorded using a 40X long-distance objective. Measurements were made over a spectral range of 100-1200 cm^{-1}, and spectra processed using LabSpec 5 software.

Visible/near-infrared reflectance (VNIR) spectra were acquired in the laboratory at wavelengths of 350 to 2500 nm using an Analytical Spectral Devices (ASD) FieldSpec3 fitted with a 5° foreoptic. The field of view was illuminated with a halogen light source at a 30° angle, the spectrometer was calibrated using a spectralon reflectance standard, and spectra were measured at an emission angle of approximately 30°. Spectra were collected from particulates for synthetic samples, and from altered cinders and rock chips for natural samples. Several tens of spectra were taken of each sample, rotated or turned between measurements, to assess heterogeneity. Field VNIR spectra were measured using a TerraSpec4 high-resolution reflectance spectrometer (Analytical Spectral Devices, Inc.) as described in Marcucci et al. (2013). Spectra were measured for wavelengths from 350 to 2500 nm with a resolution of ~3-6 nm in the visible and ~12 nm in the infrared, over a spot size of 10 mm.

Mid-infrared reflectance (MIR) spectra were acquired at 4 cm^{-1} sampling intervals on a Nicolet Magna 860 Fourier Transform Infrared (FTIR) spectrometer. Samples were first placed in a sample chamber purged of CO_2 and H_2O, and diffuse reflectance (DR) spectra were then

measured between 5000 and 400 cm^{-1} (2–25 μm) using a KBr beamsplitter and mercury cadmium telluride (MCT-B) detector. Each measurement included 1000 scans. A sample of rough aluminum was used as the reflectance standard over the whole spectral range and was assumed to have a reflectance of one. For particulate samples, additional measurements of spectra were acquired using an attenuated total reflectance (ATR) accessory, the SensIR Durascope. After acquiring a background of the crystal alone for calibration, each sample was pressed and held on a diamond crystal and spectra acquired over the wavenumber range 4000 to 400 cm^{-1} (2.5–25 μm) using a KBr beamsplitter and uncooled deuterated triglycine sulfate (DTGS) detector with a KBr window. For each sample, 50 scans per sample were made.

Several of the synthetic Fe-bearing natroalunites as well as several field and experimental samples were analyzed by Mössbauer (MB) spectroscopy. Measurements were made at room temperature using a conventional constant-acceleration spectrometer in transmission geometry with a ^{57}Co/Rh source. An α-Fe foil was used to calibrate isomer shifts and velocity scale at room temperature. The magnetic hyperfine parameters including isomer shift (IS) and quadrupole splitting (QS) were fit using the NORMOS program (Brand, 1987), which assumes a distribution of hyperfine parameters during spectral fitting.

Text tables listing the results of XRD, Raman, VNIR, MIR, and ATR measurements for the synthetic solid solution series and natural samples are deposited as supplementary materials[1].

RESULTS

Morphology and chemical composition of natural and synthetic minerals

[1] Deposit item AM-XX-XXXX, one Supplemental Figure and six Supplemental Tables. Deposit items are stored on the MSA web site and available via the *American Mineralogist* Table of Contents. Find the article in the table of contents (at GeoScienceWorld, ammin.geoscience-world.org or www.minsocam.org), and then click on the deposit link.

The Fe-bearing natroalunite found in the acid-sulfate altered deposits from Nicaragua and produced in basalt alteration experiments have a fine-grained (mostly <10 μm), pseudocubic morphology, occurring as either single crystals or as dense monomineralic crusts, mostly occurring in patches precipitated on the external surfaces of altered basalts or lining gas vesicles (Fig. 1) (McCollom et al. 2013a,b). A summary of the relative amounts of Fe and Al in the *B* site for several examples of natroalunite from natural systems and basalt alteration experiments, expressed as Fe# [=100 × Fe/(Al + Fe), molar basis], is provided in Table 2. The natural samples exhibit considerable variability in the relative proportions of Fe and Al, both between samples and for measurements of individual crystals within a single sample (the latter is reflected in the relatively large standard deviations for some samples in Table 2). Additionally, individual crystals from natural samples and from basalt alteration experiments often exhibit zonation in Fe-Al contents (Fig. 1c,f). In all of these samples, EDS and EMPA indicate that the *A* site is dominated by Na with little or no K present (McCollom et al. 2013a,b). The *A* site also appears to contain some amount of H_3O^+, but uncertainties in the measurements of Na preclude quantification of the amounts that may be present. For many of the samples listed in Table 2, the sparse distribution and small grain size precluded analysis by electron microprobe, so only compositional data from EDS are available. Although EDS is generally regarded as being semi-quantitative, comparison of measured values for Fe# determined by EDS with wet chemical and EMPA results were found to agree within 10 % (McCollom et al. 2013a).

The synthetic solid solutions have a fine-grained (20 μm or less) pseudocubic morphology very similar to that found in natural samples from volcanic environments (Fig. 3). The chemical formulas of the synthetic minerals, as determined by wet chemical methods, are listed in Table 3 (complete results of the wet chemical analyses are provided as Supplemental Table 1[1]). Based

on the wet chemistry, the synthetic minerals contain significant amounts of H_3O^+ in the *A* site, as well as deficiencies in the *B* site relative to the occupancy expected for the ideal molecular formula (Fe + Al = 3 per formula unit). Examination of the synthetic minerals by EDS indicated that they were homogenous in composition, with a narrow range of compositions found for measurements of different crystals within each sample. Only trace amounts of other phases were detected in the samples.

X-ray diffraction

Analysis of the synthetic minerals by XRD shows regular shifts in the position of many diffraction peaks with increasing Fe content (Fig. 4). For example, Fig. 4c shows a family of diffraction peaks in the vicinity of $2\theta = 30°$. With increasing Fe content, the single peak at 30.1° for endmember natroalunite shifts to lower diffraction angles and splits into two peaks for Fe# > ~60. Similarly, the prominent peak at ~18° shifts to lower values with increasing Fe, and minor peaks at ~15° and ~16° become proportionally larger (Fig. 4b). For clarity, the diffractograms shown in Fig. 4 have been adjusted to comparable vertical scales, but the overall amplitude of the peaks also decreased substantially with increasing Fe content for the same integration time. In all cases, only peaks that can be attributed to natroalunite-natrojarosite solid solution are present in the diffactograms, confirming the purity of the samples. The peaks are somewhat broad, however, which may be attributable to minor compositionally variability of the crystals owing to minor variation in Fe-Al substitution or to the relative proportion of hydronium and water in the *A* and *B* sites.

Laser Raman spectroscopy

The Raman spectra for the synthetic natroalunite-natrojarosite solid solution series exhibit two trends with increasing substitution of Fe for Al (Fig. 5). First, there is a gradual and systematic change in overall Raman spectral pattern from a typical spectrum for pure endmembers of the alunite subgroup to one characteristic of endmembers in the jarosite subgroup. For example, the natroalunite endmember (Natro6) has a doublet OH peak in the 3600-3400 cm^{-1} spectral range (Fig. 5a) and a prominent Raman peak near 1026 cm^{-1} (assigned to ν_1 of SO_4 tetrahedra, symmetric stretching vibration mode) that has the highest peak intensity in the spectral range between 1250 and 100 cm^{-1} (Fig. 5b,c). With increasing Fe, there is a transition to a triplet OH peak, the peak at ~1010 cm^{-1} becomes less prominent, and additional peaks appear in the 1180-1100 cm^{-1} range (Fig. 5a,b). The latter set of peaks has been observed for all members of the jarosite subgroup regardless of *A* site occupancy (K, Na, H_3O, NH_4, Ag, or Pb; Sasaki et al. 1998; Frost et al. 2006a; Chio et al. 2009), in which the intensities of a group of Raman peaks near 1110 cm^{-1} (assigned to ν_3 of SO_4 tetrahedra, asymmetric stretching vibration mode) are more or less equal to the intensity of ν_1 mode of SO_4 near 1010 cm^{-1}. This pattern is very different from the Raman spectra of natroalunite (Fig. 5b) and other common sulfates, such as $MgSO_4 \bullet xH_2O$ (x = 0-11), $CaSO_4 \bullet xH_2O$ (x = 0-2), and $Fe^{2+}SO_4 \bullet xH_2O$ (x = 0-7), where the ν_1 peak has much higher peak intensity than that of the ν_3 peak (Chio et al. 2006; Wang et al. 2009; Ling and Wang 2010). One possible explanation for this change in spectral pattern could be a combined effect of the smaller size of $[Fe^{3+}O_6]$ octahedron in natrojarosite (in which the Fe^{3+}-O bond lengths are between 1.98 and 2.07Å) than $[MgO_6]$, $[CaO_6]$, and $[Fe^{2+}O_6]$, and the higher degree of covalence of Fe^{3+}-O bonding than Al-O that affect the vibrations of neighboring $[SO_4]$. Second, the positions of many peaks in the Raman spectra for the solid solutions systematically shift to lower wavenumbers with increasing Fe content. This shift is

observed in all three spectral ranges: the 3600-3400 cm^{-1} range where OH Raman peaks occur (Fig. 5d), the 1200-900 cm^{-1} range where the ν_1 and ν_3 peaks of SO_4 tetrahedra occur (Fig. 5e), and below 700 cm^{-1} where the peaks from ν_3, ν_4, and lattice modes occur (Fig. 5f).

Visible/near infrared reflectance

Visible/near infrared reflectance spectra for the synthetic natroalunite-natrojarosite solid solution series exhibit absorptions due to iron electronic transitions and *M*-OH vibrations in the wavelength range 350-2500 nm. These spectral features vary systematically in intensity and position with Fe content (Fig. 6). There are four measured absorptions related to Fe electronic absorptions: a broad absorption centered at 930 nm ($^6A_{1g} \rightarrow {}^4T_{1g}$), a broad shoulder near 600 nm ($^6A_{1g} \rightarrow {}^4T_{2g}$), a strong, broad absorption near 500 nm that is the wing of the charge transfer band that is centered in the UV, and a sharp, narrow feature near 433 nm ($^6A_{1g} \rightarrow {}^4A_{1g}$, ^4E_g) (Rossman 1976; Sherman and Waite 1985; Bishop & Murad, 2005). The pure natroalunite endmember lacks the two broad absorptions, but all intermediate compositions exhibit these features, albeit with decreasing intensity as Fe content decreases. The narrow 433 nm absorption feature has been considered a sensitive indicator for the presence of jarosite (Hunt and Ashley, 1979), and is absent in the endmember natroalunite sample. Interestingly, this diagnostic feature is strongest in low Fe intermediates but weaker in higher Fe compositions, including the endmember natrojarosite, likely because of masking by the presence of a stronger absorption with a band center in the ultraviolet (UV) (Fig. 6b). As Fe content decreases, this UV band decreases in strength, resulting in an apparent increase in intensity of the 433 nm absorption. Since all of the synthetic samples had essentially the same grain size distribution, it is unlikely that grain size plays a role in the decreasing depth of this feature for higher Fe contents.

The synthetic natroalunite-natrojarosite series has three sets of vibrational absorptions at 1400-1500 nm, 1700-1900 nm, and 2100-2300 nm, which are overtones and combinations of fundamental vibrations (near 1000 cm^{-1}), related to OH bending and stretching vibrations (Bishop and Murad 2005). Natroalunite has a doublet with two absorptions of approximately equal strength at 1440 and 1492 nm, shifting to 1448 and 1491 nm as Fe content increases to Fe# = 25 (Fig. 6c). Natrojarosite has a doublet with a strong absorption at 1477 nm and a weaker shoulder near 1547 nm. Intermediate compositions with Fe# = 25-92 display a single feature that sharpens and increases in wavelength from 1452 to 1477 nm with increasing Fe content. The shoulder at ~1547 nm is distinctly evident only for the samples Fe# = 84 and above. Near 1800 nm (Fig. 6d), natroalunite exhibits a minimum at 1760 nm, natrojarosite at 1850 nm, and all samples of intermediate composition possess an absorption at 1803 nm that is strongest for intermediate iron contents. Similarly, natroalunite has a prominent absorption at 2172 nm, natrojarosite at 2268 nm, and all intermediate compositions have an absorption near 2218 nm that is most prominent for compositions near the middle of the Fe-Al range.

Mid-infrared attenuated total reflectance

Attenuated total reflectance spectra for the synthetic solid solutions are shown in Fig. 7. ATR spectra are similar to transmission spectra in that peaks are mostly dependent on the absorption coefficient, i.e., the imaginary component of the complex index of refraction, but with slightly shifted band centers and intensities. The spectra exhibit a strong ν_{OH} band center located at 3452 cm^{-1} for natroalunite and at 3351 cm^{-1} for natrojarosite (Fig. 7a), with intermediate compositions displaying a relatively systematic shift to smaller wavenumbers for higher Fe contents (Fig. 7e). The peak broadens considerably at intermediate Fe contents.

Several strong absorptions are present, centered between 1000 and 1250 cm^{-1} (peak attributions from Bishop and Murad 2005 and Lane 2007). A doublet attributable to $\nu_3(SO_4^{2-})$ stretching vibrations is observed with one center shifting systematically from 1215 to 1174 cm^{-1} as Fe content increases, while the other center occupies two discrete positions characteristic of each endmember (Fig. 7b,c). A doublet attributed to δ(OH) is also present, and its center shifts systematically from 1028 to 1007 cm^{-1} (Fig. 7d) and from 1066 to 1060 cm^{-1} with increasing Fe content, though the latter peak is not apparent in the endmember natrojarosite.

Strong absorptions are also present in the 400-650 cm^{-1} range due to a number of vibrations in the mineral structure. A doublet of $\nu_4(SO_4^{2-})$ vibrations is observed near 617 and 658 cm^{-1} for endmember natroalunite and 627 cm^{-1} and 677 cm^{-1} for endmember natrojarosite. Intermediate compositions have variable center positions, though these do not appear to vary systematically (Fig. 7a). Natroalunite has an out-of-plane bend $\gamma(OH^-)$ at 595cm^{-1}, absent in natrojarosite and more Fe-rich samples. A $\nu_2(SO_4^{2-})$ bending vibration is at 430 cm^{-1} in natroalunite, 419 cm^{-1} in intermediate compositions, and 442 cm^{-1} in natrojarosite. Lastly, *M*-O (Al, Fe) band centers are at 486 and 511 cm^{-1} in natroalunite, and 471 and 503 cm^{-1} in natrojarosite. In most intermediate samples, one band center shifts from 507 to 498 cm^{-1} and the lower wavenumber center is not discernible.

Mid-infrared reflectance

Unlike ATR spectra in the mid-infrared, MIR diffuse reflectance spectra depend strongly on both the real and imaginary components of the index of refraction, and are thus more complicated than ATR spectra (Fig. 8; Lane 2007). For wavelengths shortward of ~5-6 μm, the real component of the complex index of refraction (*n*) is approximately constant while the imaginary component of the index of refraction (*k*), proportional to absorption, varies, causing

reflectivity minima. At longer wavelengths, *n* and *k* both vary and both reflectance minima and maxima are significant in mineral identification. Thermal emission spectra from orbiters (TES & THEMIS) and rover-based instruments (MiniTES) utilize this wavelength range, and in emission data, reflectivity maxima are emissivity minima.

MIR reflectance spectra for the synthetic solid solution series are shown in Figure 8. As in ATR spectra, some of the strongest features occur at wavenumbers near 1000 cm^{-1} (Fig. 8b) (Lane 2007). These features vary with changes in the mass of the metal cation and effects on the bonding environment (Sasaki et al. 1998). The $\nu_3(SO_4^{2-})$ stretching vibration has reflectance maxima that decrease systematically from 1255 cm^{-1} in natroalunite to 1205 cm^{-1} in natrojarosite, but the second ν_3 mode varies only slightly and non-systematically between 1112 and 1118 cm^{-1}. The δ(OH) vibration is strong in natrojarosite at 1028 cm^{-1}, but is not as prominent in natroalunite or intermediates. The $\nu_4(SO_4^{2-})$ maxima in natroalunite are prominent with a doublet at 696 and 628 cm^{-1}. The latter feature is shifted to 633 cm^{-1} in Fe-rich samples with the second maximum of the doublet absent in these samples. Finally, Al/Fe-O features are strong in natrojarosite at 478 and 526 cm^{-1} but are weak to absent in natroalunite (possible feature near 520 cm^{-1}). The 598 cm^{-1} feature in natroalunite is due to an out-of-plane OH bend (Lane 2007).

A number of additional features occur in the MIR spectra in the 1500-4000 cm^{-1} range (Fig. 8a). The ν(OH) shifts systematically from ~3500 cm^{-1} for natroalunite ~3400 cm^{-1} for natrojaosite. Multiple vibrational overtones of ν_3 and $\delta(OH^-)$ occur in the 1900-2400 cm^{-1} wavenumber range (Bishop and Murad 2005). Samples with iron have a peak near 2500 cm^{-1} and the position of features comprised of the bands decreases in wavenumber with increasing Fe content.

Mössbauer spectroscopy

Two examples of the Mössbauer spectra obtained for synthetic natroalunite-natrojarosite solid solutions are shown in Fig. 9, together with a library spectrum for endmember jarosite. The synthetic samples exhibit a doublet in the MB spectra whose peak positions closely correspond to those of jarosite. Values of isomer shift (IS) and quadrapole splitting (QS) derived from the MB spectra of these and several other synthetic solid solutions are listed in Table 4 and displayed in Figure 10. For the most part, the synthetic solid solutions have MB parameters within the range of reported values for natural and synthetic jarosites, although the most Fe-enriched samples have combined IS and QS values that fall slightly outside this range. Notably, the natroalunites with relatively low Fe contents (Fe# = 10-25) have IS and QS values very similar to those reported for many jarosites. In addition, the synthetic solid solutions display decreasing values of QS with increasing Fe content, while IS shows no clear trend with Fe# (Fig. 11).

Analyses of natural deposits

In their natural setting, the Fe-bearing natroalunites found on Nicaraguan volcanoes occur both as nearly monomineralic deposits and as relatively minor phases in mixtures with other secondary minerals, most commonly amorphous silica, gypsum, and Fe-oxides/oxyhydroxides including hematite (McCollom et al. 2013b; Hynek et al. 2013). In an initial effort to evaluate the extent to which Fe-bearing natroalunite might be detectable in natural fumarolic settings, the spectral characteristics of several samples of acid-sulfate altered deposits from Nicaraguan volcanoes that were known to contain Fe-bearing natroalunite were measured and compared with results from the synthetic solid solutions (see references above for more complete descriptions of the samples and geological context). The mineral composition of the samples is summarized in Table 5, and XRD analyses of the bulk samples are provided as a Supplemental Figure 1. The

natural samples included deposits composed predominantly (>90 %) of Fe-bearing natroalunite (CN R36, Telica 7, and Masaya 3), and deposits where Fe-bearing natroalunite occurs as a relatively minor component in combination with other secondary phases (CN R21, CN R28, Telica 6). The relative proportions of Fe and Al in the natroalunites in the samples as determined by EDS and EMPA are listed in Table 2. The natroalunites in the samples range from those containing relatively small amounts of Fe (Telica 6, CN R28) to Fe-rich compositions (Telica 7, Masaya 3).

Partial X-ray diffraction patterns for the natural samples in the $2\theta = 28\text{-}31°$ range are shown in Figure 12 (the full diffraction patterns are provided as Supplemental Figure 1). All of the diffraction peaks in this range for the natural samples are shifted to lower 2θ values than that of the endmember natroalunite, consistent with Fe-for-Al substitution in the mineral structure (note that sample CN R21 has a peak for augite at ~29.8° that obscures the natroalunite peak in this region). The peak positions, however, do not align precisely with the positions expected for the measured Fe contents of the minerals, nor do they all vary systematically with measured Fe#. Potential explanations for these discrepancies include inaccurate measurements of bulk composition by EDS and EMPA (which were measured for only a limited number of crystals that may not be representative of the bulk sample), or variations in the unit cell dimensions of the natural samples relative to the synthetic solid solutions caused by additional substitutions in the *A* and *B* sites. For instance, varying degrees of deficiency in occupancy of the *B* site by Fe and Al can result in slight shifts in peak positions (e.g., Grey et al. 2013), and the natural minerals may have a different extent of deficiency at this position than the synthetic minerals. In any case, the XRD measurements exhibit shifts from the expected peak position for endmember natroalunite, and are shifted in a direction that would be indicative of Fe enrichment. The

presence of singlet peaks for the natural samples also indicates that these are true solid solutions rather than intimate, micron-scale mixtures of two separate phases like those described for some occurrences of jarosite and natrojarosite (Desborough et al. 2009).

Raman spectra for natroalunite in two samples from Cerro Negro volcano are shown in Figure 13 (CN R21, CN R36). In both cases, the spectra were obtained from analysis of single crystals of fine-grained, pseudocubic natroalunite located with the aid of a visible-light microscope; analyses of multiple crystals from the same sample yielded essentially identical spectra. The Raman spectra for both of the Cerro Negro samples show peak shifts to lower values consistent with Fe-bearing natroalunite with Fe# ≈ 10 (e.g., Fig. 13b,c). This value is slightly lower than the average Fe contents for these samples determined by EDS/EMPA, but within the range of measured values (Table 2). Also shown in the Figure 13 is a Raman spectrum measured for natroalunite produced in a laboratory simulation of acid-sulfate alteration of Cerro Negro basalt that has a substantially higher Fe content (ADSU6). The Raman peaks for this sample are shifted to even lower values than for the natural samples, reflecting the higher Fe content. In this case, the Raman peak positions are consistent with the measured amount of Fe in the sample.

VNIR spectra for several natural samples are shown in Figure 14, which includes spectra obtained both in the laboratory and in the field. The top three spectra in Figure 14a are samples composed predominantly of Fe-bearing natroalunite. These spectra all show characteristics indicative of natroalunite with minor amounts of Fe, including overall spectral shape, a doublet at ~2172 and ~2218 nm with subequal absorption depth, a doublet in the 1448-1491 nm range, a broad absorption at ~930 nm, and decreasing reflectance for wavelengths <700 nm. However, only Masaya 3 exhibits a clear absorption band at 1803 nm, a feature observed in the

intermediate synthetic solid solutions. Curiously, Masaya 3 is also the only one of these samples that displays the prominent absorption at ~433 nm seen in synthetic samples, although this feature would have been expected for all three samples based on measured Fe content (Fig. 14b). It is possible that this feature is suppressed in the other samples by absorption bands for other Fe-oxide/oxyhydroxide phases present in small amounts, which may also affect the overall shape of the spectra in the <700 nm region. The relative depths of the doublets at ~2172/2218 nm for these samples indicate Fe contents in the Fe# ≈ 15-30 range (Fig. 6e), consistent with compositions indicated by EDS and EMPA analyses.

The middle group of spectra in Figure 14 shows samples where the natroalunite is present in combination with other phases, and illustrate some of the potential complications that may arise in evaluating the composition of natroalunites that occur in mixtures. Because the spatial distribution of minerals in these samples is highly heterogeneous, it was not possible to quantitatively estimate the proportions of phases present in the field of view during spectroscopic measurements. Natroalunite is a major component of sample Telica 6, but the deposit also contains kaolinite as well as minor amounts of amorphous silica and gypsum (Hynek et al. 2013). The VNIR spectrum for this sample exhibits spectral features in the 350-1000 nm region consistent with Fe-bearing natroalunite, including a small absorption feature at 433 nm, a broad trough at ~900 nm, and the overall shape of the <700 nm region. However, the natroalunite doublet at ~2172/2218 nm is obscured by a strong absorption band from kaolinite centered at ~2205 nm, and absorptions in other regions of the spectrum reflect substantial contributions from amorphous silica and gypsum.

Natroalunite is a relatively minor phase in samples CN R21 and CN R28, where the secondary mineralogy is dominated by amorphous silica and gypsum (McCollom et al. 2013b).

The VNIR spectra for these samples are strongly influenced by contributions from these other hydrated phases. Nevertheless, sample CN R21 shows several features indicative of Fe-bearing natroalunite, including a doublet at 2190 and 2220 nm with subequal absorption depth, doublet peaks at ~1438 and ~1490 nm, a feature near 2320 nm, an absorption band at 433 nm, and a broad absorption at ~900 nm. The overall shape of the spectra at wavelengths below 1000 nm, however, appears to show some influence of the hematite that occurs in small amounts in this sample (Fig. 2). Sample CN R28 is largely composed of micron-sized natroalunite crystals distributed across the surface of large prismatic gypsum crystals. The spectra indicate a substantial contribution from gypsum, but the shape of the spectra in the 2140-2290 nm and <1000 nm region has some attributes of natroalunite-natrojarosite except for the absence of the 433 nm feature. However, the shape of these features is most similar to solid solutions with Fe# ≈ 50, which is much higher than the Fe contents indicated by EDS and XRD analysis (Table 2; Fig. 12). It is likely that the spectral features in the region are influenced by the presence of gypsum and other minerals in the sample, obscuring the contribution from natroalunite.

The MIR spectra of three natural samples are shown in Figure 15. The spectra exhibit several SO_4 and OH vibration features indicative of the presence of sulfate and hydroxylated minerals. However, features that are uniquely indicative of the presence of natroalunite or its Fe contents are not obvious in all samples. The presence of small reflectance peaks at ~1255 cm^{-1} and the absence of a peak at 1028 cm^{-1} are both consistent with natroalunite with Fe# <~25. The broad peak at ~2500 cm^{-1} is consistent with the presence of an Fe-bearing member of the natroalunite-natrojarosite series, but provides no specific information about the Fe content. Potentially diagnostic features in the 400-700 cm^{-1} are only weakly present in sample CN R36, and not evident in the other samples. Specific assignment of any of these features to natroalunite

would require linear unmixing models to evaluate potential contributions from other phases present in the samples.

A Mössbauer spectrum for one of the natural samples (CN R21) is shown in Figure 9. Deconvolution of this and other spectra for altered basalt cinders from Cerro Negro identified an alunite group component in addition to several other primary and secondary Fe-bearing phases, and similar results were found for examples of altered basalt cinders from laboratory experiments (McCollom et al. 2013a,b). Mössbauer parameters derived for the Fe-bearing natroalunite component of three natural samples from Cerro Negro as well as several products of laboratory simulations of acid-sulfate alteration are shown in Figures 10 and 11. The natural and experimental samples exhibit a considerable range of IS and QS values. Values of IS for the natural and experimental samples are generally slightly higher than those determined for the synthetic solid solution. The experimental samples and one of the Cerro Negro samples have QS values similar to that of the synthetic solid solutions with relatively low Fe contents (1.15-1.25 mm/s), but two of the CN samples have substantially lower QS values (0.99-1.06 mm/s) more similar to solid solutions with high Fe contents (1.05-1.11 mm/s). In one of these samples (CN R21), the average Fe content for natroalunite is Fe# = 17, while the other appears to have a bimodal distribution of minerals in the alunite group ranging from Fe-rich natroalunite (Fe# ≈ 20-30) to Al-rich natrojarosite (Fe# ≈ 60-50) (see McCollom et al. 2013b). For both the natural and experimental samples, values of IS and QS fall within the range of previously reported values for natural and synthetic members of the jarosite subgroup (Fig. 10; Table 4).

DISCUSSION

Determination of relative Fe-Al contents of alunite-jarosite group minerals

All of the methods used to investigate natroalunite-natrojarosite solid solutions exhibited systematic variations in spectral patterns and peak positions with Fe content that could potentially be used to infer the composition of natural minerals in this group, either on Earth or in other planetary contexts. Of course, development of a comprehensive calibration to infer the compositions of solid solutions among these minerals using spectral or XRD methods will require further investigation of the impact of additional compositional factors (e.g., Swayze et al. 2008). For instance, solid solution mixing of Na, K, and H_3O^+ on the *A* site is common in minerals from this group, and many natural minerals in the alunite and jarosite subgroups that precipitate in low temperature environments also have deficiencies in occupancy of the *B* site relative to the ideal molecular formula (Stoffregen et al. 2000; Grey et al. 2013). Inclusion of additional H_2O into the crystal structure to compensate for these deficiencies can result in lowering the symmetry of the minerals from rhombohedral to monoclinic (Scarlett et al. 2010; Grey et al. 2011, 2013). Further work will be required to determine how these and other factors impact the spectral and XRD characteristics of minerals from this group. Nevertheless, at least for the case of laser Raman spectroscopy, previous studies (e.g., Murphy et al. 2009) have indicated that substitutions in the *A* site result in only small shifts in peak position relative to those observed here for Fe-Al substitutions in the *B* site, which appear to have a much larger influence on the vibrations of [SO4] and [OH] groups. In addition, investigation of the variation of peak positions on ambient environmental conditions such as temperature may be required to employ these methods on Mars or other planetary surfaces (e.g., Mills et al. in review).

As demonstrated by the analysis of natural samples, a potential limitation on the use of these methods to identify and evaluate the composition of minerals in the alunite and jarosite subgroups are interferences from other phases that are likely to be present in many acid-sulfate

deposits. These additional phases can inhibit both the detection of minerals from this group and the capacity to infer their composition. For instance, kaolinite and other Al-phyllosilicates have absorption bands in the ~2200 nm region of the VNIR spectra that overlap with the diagnostic features of natroalunite/natrojarosite in this region (Fig. 14c), and gypsum may interfere with detection of absorbance bands in the 1400-1500 nm and 1750-1850 nm regions. Similarly, hematite and other Fe-oxides/oxyhydroxides have absorption bands in the VNIR spectral region below 1000 nm that can obscure diagnostic features for Fe-bearing minerals in the alunite group and their compositions (Fig. 14b).

Conversely, the overlap in spectral bands with other minerals presents the possibility for misidentification of phases if spectra for solid solutions in the alunite group are not considered. For example, the increasing band depth at ~2218 nm in VNIR spectrum with increasing Fe content observed for natroalunite-natrojarosite solid solutions could lead to spectral properties that could be mistaken for kaolinite or other Al-phyllosilicates. It is worth noting, however, that there is a slight difference between the position of the absorption feature for intermediate natroalunite-natrojarosite compositions at ~2218 nm and that of kaolinite at ~2205 nm. Telica 6, which is the only natural sample shown in Figure 14 where kaolinite was identified during XRD and SEM/EDS analysis, is the only sample with a feature centered at ~2205 nm, while the other natural samples have features in this region shifted to slightly higher wavelengths consistent with Fe-bearing natroalunite. Potentially, this shift could be used to differentiate between kaolinite and Fe-bearing natroalunite during spectral analysis, provided that the position of the absorbance feature at ~2218 nm does not shift significantly with other compositional variables (such as substitution of H_3O^+ for Na in the *A* site). In addition, the sharp 433 nm absorption band of VNIR spectra is often considered to be diagnostic for the presence of jarosite, but in the solid

solution spectra this band was observed in Fe-bearing natroalunites and decreased in magnitude with increasing Fe content. Consequently, detection of this band could be consistent with any Fe-bearing member of the alunite group, not just those in the jarosite subgroup. Together, these observations indicate that it would be very worthwhile to include solid solutions from the alunite mineral group in reference libraries for interpretation of spectral data from Mars and elsewhere.

Examination of the natural samples by VNIR indicates that identification of natroalunite-natrojarosite solid solutions and estimation of their Fe-content should be relatively straightforward in samples where they dominate the mineralogy in the field of view. Significant complications may arise, however, when they occur in mixtures with other minerals including Fe-oxides/oxyhydroxides, phyllosilicates, other hydrated sulfate minerals, and hydrated forms of silica. Since these are precisely the types of minerals that would be expected to co-occur with natroalunite/natrojarosite (and other minerals in the alunite/jarosite subgroups) in natural acid-sulfate environments, a key objective for future work involving solid solutions will be to evaluate the extent to which they may be masked by accessory phases. In addition, a better understanding of how the presence of other Fe-bearing phases leads to suppression of the 433 nm feature would aid interpretation of spectra in the <1000 nm region.

Laser Raman spectroscopy appears to have a high potential to provide compositional information for solid solutions in the alunite and jarosite subgroups, particularly during in situ Raman measurements where the spectrum is obtained from a single mineral phase excited by a well-focused laser beam (10-20 μm diameter) during planetary surface exploration. Complications may arise in cases where mineral grain size is less than the spot size of the laser beam, allowing multiple phases to be present in the field of view. However, this problem may be less severe than in the cases of VNIR and MIR because of the sharpness of Raman spectral peaks

and less extensive overlap for different phases, especially because of the very different peak positions (on the order of a few hundreds in wavenumber) for sulfates, silicates, and Fe-oxides/oxyhydroxides.

The Mössbauer results do not show any consistent variation in either QS or IS with increasing Fe content. Values of these parameters are shown in Figure 11 for the samples discussed here as well as a few additional samples from the literature where compositional data are available. While our synthetic solid solutions display decreasing values of QS with increasing Fe content, other samples do not. Morris et al. (2006) suggested that substitution of Al for Fe in members of the jarosite family would increase quadrapole splitting, evidently because two Al-bearing jarosites included in their study had QS values near the high end of the range reported in the literature (Fig. 11). However, other samples with higher Al contents do not have QS values higher than the Al-bearing jarosites.

As a consequence, it appears that Mössbauer spectroscopy may not be a particularly useful method for determining the Fe content of minerals in the alunite-jarosite group. To the contrary, the apparent insensitivity of MB spectroscopy to Fe contents suggests that it is not possible to differentiate Fe-bearing natroalunite from members of the jarosite family using this method, even when only a few mole% Fe is present in the *B* site. Indeed, a doublet in a MB spectrum with QS ≈ 1.05-1.25 and IS ≈ 0.36-0.40 may be sufficient only to indicate the presence of an Fe-bearing mineral in the alunite group, without providing more specific information about the identity or composition of the phase.

Implications for sulfate deposits on Mars

Minerals from the alunite group have been inferred to be present at several locations across Mars based on interpretation of data from orbital remote sensing and surface exploration.

Members of the jarosite subgroup have been reported to be present in the layered sulfate deposits at the Opportunity rover landing site in Meridiani Planum based on results from Mössbauer spectroscopy (Klingelhöfer et al. 2004), and may be present at the Gusev Crater landing site as well (Morris et al. 2008). The use of high spatial and spectral resolution instruments from Mars orbit has led to additional reported detections of alunite (Swayze et al. 2008a; Wray et al. 2011) and jarosite (Milliken et al. 2008; Farrand et al. 2009; Wray et al. 2011; Ehlmann and Mustard, 2012; Thollot et al. 2012) from multiple additional locations on the Martian surface, in regionally significant deposits. For example, Farrand et al. (2009) noted occurrences of jarosite near Al-phyllosilicates in Mawrth Vallis and this assemblage possibly reflects early hydrothermal alteration of Mars' crust. Elsewhere, alunite and kaolinite have been reported in putative acid-saline paleolake deposits within craters in Terra Sirenum (Swayze et al. 2008b; Wray et al. 2011). All of these interpretations of orbital data, however, are based on endmember spectra, and consideration of spectra for intermediate solid solutions may lead to additional identifications as well as providing constraints on the chemical composition of phases in this mineral group where they have already been identified.

Several of the spectroscopic methods investigated in this study have the potential to be useful to identify intermediate Fe-Al solid solutions from the alunite group on Mars, and to infer their chemical composition. The reflectance VNIR spectra obtained in this study are relevant to OMEGA and CRISM onboard the Mars Express and MRO orbiters. The systematic changes in XRD patterns with varying Fe-Al content should provide also useful information for the CheMin instrument onboard the Curiosity rover if members of the alunite group are encountered in Gale Crater. Flight models of a laser Raman spectrometer are under development (Wang et al. 2003), and one of them was selected for the ExoMars rover (a mission run by the European Space

Agency scheduled for launch in 2018). Future research should allow development of calibration curves for evaluation for solid solution compositions using all of these methods.

There are several outstanding problems in Mars exploration where consideration of intermediate compositions may be relevant to regional studies. For example, multi-component fits of thermal emission spectra (MiniTES) from the sulfate-bearing bedrock at Meridiani Planum were not significantly improved by inclusion of endmember jarosite at the level inferred from Mössabauer results (10%) (Glotch et al. 2006). However, MB spectra of solid solutions indicate that the component interpreted as jarosite could be equally well represented by Fe-bearing natroalunite or other members of the natroalunite subgroup (Fig. 10), suggesting that models of Meridiani mineralogy should be expanded to consider solid solutions encompassing the entire alunite group. The synthetic minerals with compositions intermediate between natroalunite and natrojarosite exhibit distinctive spectral characteristics at MiniTES wavelengths (1600-200 cm^{-1}) (Fig. 8), and including solid solutions in the reference library could potentially improve fits to the observed MiniTES spectra.

As a second example, a "doublet material" with absorptions at 2205–2218 nm and 2265–2278 nm has been identified in CRISM data from several areas but has not yet been associated with a particular mineral (Roach et al. 2010; Weitz et al. 2012; Thollot et al. 2012). The position of these features correspond closely to those of the synthetic natroalunite-natroajarosite solid solutions containing relatively high Fe, suggesting that they could be consistent with the presence of a member of the alunite group with an intermediate composition of Fe# ≈ 65. The "doublet material" has additional absorptions at 1400-1420 nm and 1910-1920 nm that are not observed in spectra for the pure natroalunite-narojarosite series, so further work will be required to determine whether mixtures with additional phases such as hydrated silica, gypsum, and

hematite can reproduce the observed spectra. In this respect, it may be worth noting that in most instances the natroalunite at Cerro Negro is found in close association with amorphous silica and gypsum, and samples of these deposits exhibit features in the 1400 and 1910 nm regions (e.g., CN R21 and CN R28; Fig. 14). In addition, the presence of Al-phyllosilicates has been inferred in some locations based on absorptions at 2170 and 2210 nm that are characteristic of the kaolinite doublet, but with the relative intensities of these features reversed from what is expected for kaolinite (Fig. 14c). As an alternative, these spectral features could potentially be explained by Fe-bearing natroalunite. Whether natroalunite-natrojarosite solid solutions can account for these and other features will require detailed comparisons of martian spectra with spectra obtained for synthetic minerals, but these possibilities raise the prospect that alunite group minerals with intermediate Fe compositions could be widespread on the surface of Mars.

ACKNOWLEDGEMENTS

This research was supported by funds from NASA Mars Fundamental Research Program grants NNX12AI02G (TMM) and NNX10AM89G (AW), NASA Exobiology Award #NNX08AQ11G (TMM and BMH), and NASA Early Career Award #NNX12AF20G (BMH). Thanks to George Rossman for assistance and use of his FTIR spectrometer and to Frieder Klein for help with the Raman analysis of natural samples. The authors are grateful for reviews by Gregg Swayze and Stuart Mills, whose thoughtful comments helped to improve the manuscript.

References

Bishop, J.L., and Murad, E. (2005) The visible and infrared spectral properties of jarosite and alunite. American Mineralogist, 90, 1100-1107.

Blake, D., Vaniman, D., Achilles, C., Anderson, R., Bish, D., Bristow, T., Chen, C., Chipera, C., Crisp, J., Des Marais, D., Downs, R.T., Farmer, J., Feldman, S., Fonda, M., Gailhanou, M., Ma, H., Ming, D.W., Morris, R.V., Sarrazin, P., Stolper, E., Treiman, A., and Yen, A. (2012) Characterization and calibration of the CheMin mineralogical instrument on Mars Science Laboratory. Space Science Reviews, 170, 341-399.

Brand, R.A. (1987) Improving the validity of hyperfine field distributions from metallic alloys. Part I: Unpolarized source. Nuclear Instruments and Methods in Physics Research B, 28, 398-405.

Brophy, G.P., Scott, E.S., and Snellgrove, R.A. (1962) Sulfate studies II: Solid solution between alunite and jarosite. American Mineralogist, 47, 112-126.

Chio, C.H., Sharma, S.K., Ming, L., and Muenow, D.W. (2005) Micro-Raman studies of hydrous ferrous sulfates and jarosites. Spectrochimica Acta Part A, 61, 2428–2433.

Chio, C.H., Sharma, S.K., Ming, L., and Muenow, D.W. (2009) Raman spectroscopic investigation on Jarosite-Yavapaiite stability. Spectrochimica Acta Part A, 75, 162-71.

Desborough, G.A., Smith, K.S., Lowers, H.A., Swayze, G.A., Hammarstrom, J.M., Diehl, S.F., Leinz, R.W., and Driscoll, R.L. (2010) Mineralogical and chemical characteristics of some natural jarosites. Geochimica et Cosmochimica Acta 74, 1041-1056.

Dutrizac, J.E., and Jambor, J.L. (2000) Jarosites and their application in hydrometallurgy. In C. N. Alpers, J. L. Jambor, and D. K. Nordstrom, Eds. Sulfate Minerals: Crystallography, Geochemistry, and Environmental Significance. Reviews in Mineralogy and Geochemistry, Mineralogical Society Of America, Washington, D. C., pp. 405-452.

Ehlmann, B.L., and Mustard, J.F. (2012) An in-situ record of major environmental transitions on early Mars at Northeast Syrtis Major. Geophysical Research Letters, 39, L11202, doi:10.1029/2012GL051594.

Elwood Madden, M.E., Madden, A.S., and Rimstidt, J.D. (2009) How long was Meridiani Planum wet? Applying a jarosite stopwatch to determine the duration of aqueous diagenesis. Geology, 37, 635-638.

Elwood Madden, A.S., Rimstidt, J.D., Zahrai, S., Kendall, M.R., and Miller, M.A. (2012) Jarosite dissolution rates and nanoscale mineralogy. Geochimica Cosmochimica Acta, 91, 306-312.

Farrand, W.H., Glotch, T.D., Rice, Jr., J.W., Hurowitz, J.A., and Swayze, G.A. (2009) Discovery of jarosite within the Mawrth Vallis region of Mars: Implications for the geologic history of the region. Icarus, 204, 478–488.

Frost, R., Wills, R., Weier, M.L., Martens, W., and Mills, S. (2006a) A Raman spectroscopic study of selected natural jarosites. Spectrochimica Acta Part A, 63, 1-8.

Frost, R., Wills, R., Weier, M.L., Martens, W., and Kloprogge, J.T. (2006b) A Raman spectroscopic study of alunites. Journal of Molecular Structure, 785, 123-132.

Glotch, T.D., Bandfield, J.L., Christensen, P.R., Calvin, W.M., McLennan, S.M., Clark, B.C., Rogers, A.D., and Squyres, S.W. (2006) Mineraology of the light-toned outcrop at Meridiani Planum as seen by the Miniature Thermal Emission Spectrometer and

implications for its formation. Journal of Geophysical Research, 111, E12S03, doi:10.1029/2005JE002672.

Golden, D.C., Ming, D.W., Morris, R.V., and Graff, T.G. (2008) Hydrothermal synthesis of hematite spherules and jarosite: Implications for diagenesis and hematite spherule formation in sulfate outcrops at Meridiani Planum, Mars. American Mineralogist, 93, 1201–1214.

Grey, I.E., Scarlett, N.V.Y., Bordet, P., and Brand, H.E.A. (2011) Jarosite-butlerite intergrowths in non-stoichiometric jarosites: crystal chemistry of monoclinic natrojarosite-hydroniumjarosite phases. Mineralogical Magazine, 75, 2775-2791.

Grey, I.E., Scarlett, N.V.Y., and Brand, H.E.A. (2013) Crystal chemistry and formation mechanism of non-stoichiometric monoclinic K-jarosites. Mineralogical Magazine, 77, 249-268.

Härtig, C., Brand, P., and Bohmhammel, K. (1984) Fe-Al-Isomorphie und Strukturwasser in Kristallen vom Jarostie-Alunit-Typ, Zeitschrift fur Anorganische und Allgemeine Chemie, 508, 159-164.

Hrynkiewicz, A.Z., Kubisz, J., and Kulgawczuk, D.S. (1965) Quadrupole splitting of the 14.4 gamma line of 57Fe in iron sulfates of the jarosite group. Journal of Inorganic and Nuclear Chemistry, 27, 2513– 2517.

Hunt, G.R. and Ashley, R.P. (1979) Spectra of altered rocks in the visible and near infrared. Economic Geology, 74, 1613–1629.

Hynek, B.M., McCollom, T.M., Marcucci, E.C., Brugman, K. and Rogers, K.L. (2013) Assessment of environmental controls on acid-sulfate alteration at active volcanoes in Nicaragua: Applications to relic hydrothermal systems on Mars. Journal of Geophysical Research - Planets, 118, doi:10.1002/jgre.20140.

Johnson, J.H. (1977) Jarosite and akaganeite from White Island volcano, New Zealand: An X-ray and Mossbauer study. Geochimica Cosmochimica Acta, 41, 539– 544.

Klingelhöfer, G., Morris, R.V., Bernhardt, B., Schröder, C., Rodionov, D.S., de Souza, P.A., Yen, A., Gellert, R., Evlanov, E.N., Zubkov, B., Foh, J., Bonnes, U., Kankeleit, E., Gu□tlich, P., Ming, D.W., Renz, F., Wdowiak, T., Squyres, S.W., and Arvidson, R.E. (2004) Jarosite and hematite at Meridiani Planum from Opportunity's Mössbauer spectrometer. Science, 306, 1740–1745.

Lane, M.D. (2007) Mid-infrared emission spectroscopy of sulfate and sulfate-bearing minerals. American Mineralogist, 92, 1–18.

Ling, Z.C., and Wang, A. (2010) A systematic spectroscopic study of eight hydrous ferric sulfates relevant to Mars. Icarus, 209, 422-433.

Marcucci, E.C., Hynek, B.M., Kierein-Young, K.S. and Rogers, K.L. (2013) Visible-near infrared reflectance spectroscopy of volcanic acid-sulfate alteration in Nicaragua: Analogs for early Mars. Journal of Geophysical Research - Planets, 118, doi:10.1002/jgre.20159.

Maubec, N., Lahfid, A., Lerouge, C., Willie, G., and Michel, K. (2012) Characterization of alunite supergroup minerals by Raman spectroscopy. Spectrochimica Acta A, 96, 925-939.

McCollom, T.M., Robbins, M., Moskowitz, B., Berquó, T.S., Jöns, N., and Hynek, B.M. (2013a) Experimental study of acid-sulfate alteration of basalt and implications for sulfate deposits on Mars. Journal of Geophysical Research, 118, 1-38.

McCollom, T.M., Hynek, B.M., Rogers, K., Moskowitz, B., and Berquó, T.S. (2013b) Chemical and mineralogical trends during acid-sulfate alteration of pyroclastic basalt at Cerro Negro volcano and implications for early Mars. Journal of Geophysical Research, 118, 1719-1751.

Milliken, R.E., Swayze, G.A., Arvidson, R.E., Bishop, J.L., Clark, R.N., Ehlmann, B.L., Green, R.O., Grotzinger, J.P., Morris, R.V., Murchie, S.L., Mustard, J.F., and Weitz, C. (2008) Opaline silica in young deposits on Mars. Geology, 36, 847–850.

Mills, S. J., Hatert, F., Nickel, E. H., and Ferraris, G. (2009) The standardization of mineral group hierarchies. European Journal of Mineralogy, 21, 1073-1080.

Morris, R.V., Klingelhöfer, G., Schröder, C., Rodionov, D.S., Yen, A., Ming, D.W., de Souza, Jr., P.A., Wdowiak, T., Fleischer, I., Gellert, R., Bernhardt, B., Bonnes, U., Cohen, B.A., Evlanov, E.N., Foh, J., Gu□tlich, P., Kankeleit, E., McCoy, T., Mittlefehldt, D.W., Renz, F., Schmidt, M.E., Zubkov, B., Squyres, S.W., and Arvidson, R.E. (2006) Mossbauer mineralogy of rock, soil, and dust at Meridiani Planum, Mars: Opportunity's journey across sulfate-rich outcrop, basaltic sand and dust, and hematite lag deposits. Journal of Geophysical Research, 111, doi:10.1029/ 2006JE002791.

Morris, R.V., Klingelhöfer, G., Schröder, C., Fleischer, I., Ming, D.W., Yen, A.S., Gellert, R., Arvidson, R.E., Rodionov, D.S., Crumpler, L.S., Clark, B.C., Cohen, B.A., McCoy, T.J., Mittlefehldt, D.W., Schmidt, M.E., de Souza, Jr., P.A., and Squyres, S.W. (2008) Iron mineralogy and aqueous alteration from Husband Hill through Home Plate at Gusev Crater, Mars: Results from the Mössbauer instrument on the Spirit Mars Exploration Rover. Journal of Geophysical Research, 113, E12S42, doi:10.1029/2008JE003201.

Murphy, P.J., Smith, A.M.L., Hudson-Edwards, K.A., Dubbin, W.E., and Wright, K. (2009) Raman and IR spectroscopic studies of alunite-supergroup compounds containing Al, Cr^{3+}, Fe^{3+} and V^{3+} at the *B* site. Canadian Mineralogist, 47, 663–681.

Papike, J. J., Karner, J. M., and Shearer, C. K. (2006) Comparative planetary mineralogy: Implications of martian and terrestrial jarosite. A crystal chemical perspective. Geochimica Cosmochimica Acta, 70, 1309-1321.

Papike, J.J., Burger, P.V., Karner, J.M., Shearer, C.K., and Lueth, V.W. (2007) Terrestrial analogs of martian sulfates: Major, minor element systematic and Na-K zoning in selected samples. American Mineralogist, 92, 444-447.

Papike, J.J., Karner, J.M., Shearer, C.K., and Burger, P.V. (2009) Silicate mineralogy of martian meteorites. Geochimica Cosmochimica Acta, 73, 7443-7485.

Ripmeester, J.A., Ratcliffe, C.I., Dutrizac, J.E., and Jambor, J.L. (1986) Hydronium ion in the alunite-jarosite group. Canadian Mineralogist, 24, 435-447.

Roach, L.H., Mustard, J.F., Swayze, G., Milliken, R.E., Bishop, J.L., Murchie, S.L., and Lichtenberg, K. (2010) Hydrated mineral stratigraphy of Ius Chasma, Valles Marineris. Icarus, 206, 253–268.

Rossman, G.R. (1976) Spectroscopic and magnetic studies of ferric iron hydroxyl sulfates: the series $Fe(OH)SO_4 \cdot nH_2O$ and the jarosites. American Mineralogist, 61, 398–404.

Sasaki, K., Tanaike, O., and Konno, K. (1998) Distinction of jarosite-group compounds by raman spectroscopy. Canadian Mineralogist, 36, 1225-1235.

Scarlett, N.V.Y., Grey, I.E., and Brand, H.E.A. (2010) Ordering of iron vacancies in monoclinic jarosites. Amercian Mineralogist, 95, 1590-1593.

Scott, K.M. (1987) Solid solution in, and classification of, gossan-derived members of the alunite-jarosite family, northwest Queensland, Australia. American Mineralogist, 72, 178-187.

Serna, C.J., Parada Cortina, C., and Garcia Ramos, J.V. (1986) Infrared and Raman study of

alunite—jarosite compounds. Spectrochimica Acta Part A, 42, 729–734.

Sherman, D.M. and Waite, T.D. (1985) Electronic spectra of Fe3+ oxides and oxide hydroxides in the near IR to near UV. American Mineralogist, 70, 1262–1269.

Stoffregen, R.E., and C.N. Alpers (1992) Observations on the unit-cell dimensions, H_2O contents, and δD values of natural and synthetic alunite. American Mineralogist, 77, 1092-1098.

Stoffregen, R.E., Alpers, C.N., and Jambor, J. L. (2000) Alunite-jarosite crystallography, thermodynamics, and geochronology. In C.N. Alpers, J.L. Jambor, and D.K. Nordstrom, Eds. Sulfate Minerals: Crystallography, Geochemistry, and Environmental Significance. Reviews in Mineralogy and Geochemistry, Mineralogical Society Of America, Washington, D. C., pp. 453-479.

Swayze, G.A., Desborough, G.A., Smith, K.S., Lowers, H.A., Hammarstrom, J.M., Diehl, S.F., Leinz, R.W., and Driscoll, R.L. (2008a) Understanding jarosite—From mine waste to Mars. In P.L. Verplanck, Ed. Understanding Contaminants Associated With Mineral Deposits, United States Geological Survey Circular, 1328, 8–13.

Swayze, G.A., Ehlmann, B.L., Milliken, R.E., Poulet, F., Wray, J.J., Rye, R.O., Clark, R.N., Desborough, G.A., Crowley, J.K., Gondet, B., Mustard, J.F., Seelos, K.D., and Murchie, S.L. (2008b), Discovery of the acid-sulfate mineral alunite in Terra Sirenum, Mars, using MRO CRISM: Possible evidence for acid-saline lacustrine deposits? Eos Transactions of the American Geophysical Union, 89(53), Fall Meeting Supplement, Abstract P44A–04.

Thollot, P., Mangold, N., Ansan, V., Le Mouélic, S., Milliken, R.E., Bishop, J.L., Weitz, C.M., Roach, L.H., Mustard, J.F., and Murchie, S. L. (2012) Most Mars minerals in a nutshell:

Various alteration phases formed in a single environment in Noctis Labyrinthus. Journal of Geophysical Research, 117, E00J06, doi:10.1029/2011JE004028.

Wang, A. (2012) In situ laser Raman Spectroscopy for Mars Sample Return Mission. 43rd Lunar and Planetary Science Conference, abstract #2149.

Wang, A., Haskin, L.A., Lane, A.L., Wdowiak, T.J., Squyres, S.W., Wilson, R.J., Hovland, L.E., Manatt, K.S., Raouf, N., and Smith, C.D. (2003) Development of the Mars Microbeam Raman Spectrometer (MMRS). Journal of Geophysical Research, 108, 5005, doi:10.1029/2002JE001902.

Wang, A., Freeman, J. J., and Jolliff, B. L. (2009) Phase transition pathways of the hydrates of magnesium sulfate in the temperature range 50ºC to 5ºC: Implication for Sulfates on Mars. Journal of Geophysical Research, 114, doi:10.1029/2008JE003266.

Weitz, C.M., Noe Dobrea, E.Z., Lane, M.D., and Knudson, A.T. (2012) Geologic relationship between gray hematite, sulfates, and clays in Capri Chasma. Journal of Geophysical Research, 117, E00J09, doi:10.1029/ 2012JE004092.

Wray, J.J., Milliken, R.E., Dundas, C.M., Swayze, G.A., Andrews-Hanna, J.C., Baldridge, A.M., Chojnacki, M., Bishop, J.L., Ehlmann, B.L., Murchie, S.L., Clark, R.N., Seelos, F.P., Tornabene, L.L., and Squyres, S.W. (2011) Columbus crater and other possible groundwater-fed paleolakes of Terra Sirenum, Mars. Journal of Geophysical Research, 116, E01001, doi:10.1029/2010JE003694.

Table 1. Ideal end-member molecular formulas for common minerals from the alunite group.

End-member	Formula
Alunite subgroup (Al > Fe)	
Alunite	$KAl_3(SO_4)_2(OH)_6$
Natroalunite	$NaAl_3(SO_4)_2(OH)_6$
Jarosite subgroup (Fe > Al)	
Jarosite	$KFe_3(SO_4)_2(OH)_6$
Natrojarosite	$NaFe_3(SO_4)_2(OH)_6$
Hydroniumjarosite	$(H_3O^+)Fe_3(SO_4)_2(OH)_6$

Table 2. Relative Fe-Al contents of Fe-bearing natroalunites (expressed as Fe#) in natural samples from Cerro Negro, Telica, and Masaya volcanoes, Nicaragua, and from a laboratory simulation of acid-sulfate alteration of basalt (ADSU6).

Sample	Method	*n*	Average Fe# (std. dev.)
CN R21	EDS	24	17 (12)
	EMPA	10	16 (6)
CN R36	EDS	10	15 (12)
	EMPA	14	16 (2)
	XRF[#]	2	16.7 (0.1)
CN R28	EDS	9	6 (1)
Telica 6	EDS	14	4 (2)
Telica 7	EDS	38	26 (16)
Masaya 3	EDS	14	39 (14)
ADSU6	EMPA	26	38 (5)

Fe# = 100 × [Fe/(Fe + Al)], molar basis. *n* = number of analyses. [#]Bulk rock analysis of sample CN R36, which is composed predominantly (>90%) of natroalunite (McCollom et al. 2013b).

Table 3. Calculated molecular formulas of synthetic natroalunite-natrojarosite solid solutions based on wet chemical analyses (see McCollom et al. 2013a).

Sample	Calculated Formula	Fe#
Natro6	$(Na_{0.82}H_3O^+_{0.18})Al_{2.69}(SO_4)_2(OH)_{5.07}(H_2O)_{0.93}$	0
Natro8	$(Na_{0.89}H_3O^+_{0.11})(Al_{2.59}Fe_{0.30})(SO_4)_2(OH)_{5.67}(H_2O)_{0.33}$	10
Natro4	$(Na_{0.96}H_3O^+_{0.04})(Al_{2.36}Fe_{0.60})(SO_4)_2(OH)_{5.88}(H_2O)_{0.12}$	20
Natro2	$(Na_{0.87}H_3O^+_{0.13})(Al_{2.10}Fe_{0.70})(SO_4)_2(OH)_{5.40}(H_2O)_{0.60}$	25
Natro7	$(Na_{0.88}H_3O^+_{0.12})(Al_{1.57}Fe_{1.48})(SO_4)_2(OH)_{6.15}$	49
Natro1	$(Na_{0.91}H_3O^+_{0.09})(Al_{1.15}Fe_{1.79})(SO_4)_2(OH)_{5.82}(H_2O)_{0.18}$	61
Natro3	$(Na_{0.90}H_3O^+_{0.10})(Al_{1.00}Fe_{1.89})(SO_4)_2(OH)_{5.67}(H_2O)_{0.33}$	65
Natro14	$(Na_{0.84}H_3O^+_{0.16})(Al_{0.45}Fe_{2.40})(SO_4)_2(OH)_{5.55}(H_2O)_{0.45}$	84
Natro10	$(Na_{0.86}H_3O^+_{0.14})(Al_{0.22}Fe_{2.51})(SO_4)_2(OH)_{5.19}(H_2O)_{0.81}$	92
Natro9	$(Na_{0.93}H_3O^+_{0.10})Fe_{2.96}(SO_4)_2(OH)_{5.88}(H_2O)_{0.12}$	100

Table 4. Room temperature magnetic hyperfine Mössbauer parameters for synthetic Fe-bearing natroalunite.

	QS (mm/s)	IS (mm/s)	%
Natro8 (Fe#=10)	1.24(1)	0.36(1)	100
Natro4 (Fe#=20)	1.23(1)	0.38(1)	100
Natro2 (Fe#=25)	1.19(1)	0.36(1)	100
Natro1 (Fe#=61)	1.12(1)	0.36(1)	100
Natro14 (Fe#=84)	1.06(1)	0.35(1)	100
Natro10 (Fe#=92)	1.11(1)	0.36(1)	100
Natro9 (Fe#=100)	1.05(1)	0.35(1)	100

QS = quadrupole splitting and IS = isomer shift. Errors are quoted in parenthesis. Mössbauer parameters were fit with single components in all cases.

Table 5. Mineral composition of acid-sulfate fumarole deposits from Nicaraguan volcanoes containing Fe-bearing natroalunites (*M* = major, *m* = minor, *t* = trace), as determined by a combination of XRD and SEM/EDS analysis.

Sample	Phases present
CN R21	Glass (*M*), amorphous silica (*M*), plagioclase (*m*), augite (*m*), natroalunite (*m*), gypsum (*m*), magnetite (*t*), FeOx (*t*)
CN R36	Natroalunite (*M*), amorphous silica (*t*)
CN R28	Gypsum (*M*), natroalunite (*M*), amorphous silica (*m*), FeOx (*t*)
Telica 6	Natroalunite (*M*), kaolinite (*m*), amorphous silica (*m*)
Telica 7	Natroalunite (*M*), amorphous silica (*m*)
Masaya 3	Natroalunite (*M*), amorphous silica (*m*)
ADSU6	Glass (*M*), amorphous silica (*M*), plagioclase (*m*), augite (*m*), anhydrite (*m*), natroalunite (*m*), hematite (*t*), FeOx (*t*)

Relative abundances estimated from XRD and SEM analysis based on: $M \approx$ 10-90%, $m \approx$ 2-10%, $t <$ ~2%. FeOx = unidentified micron- to submicron-sized iron oxide/oxyhydroxides.

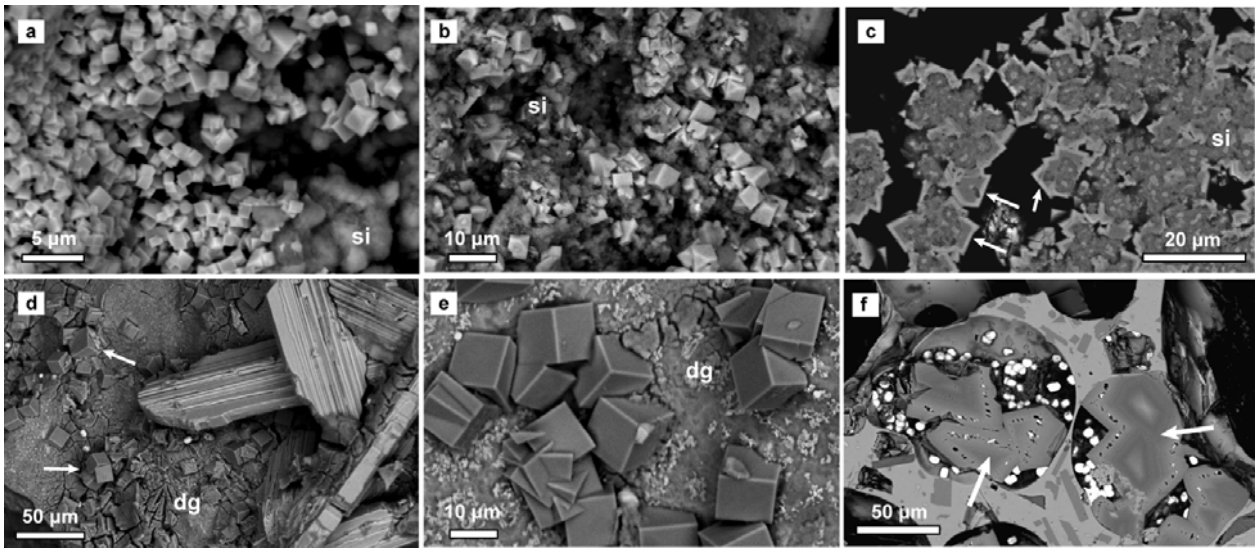

Figure 1. Backscattered electron images of representative pseudocubic Fe-bearing natroalunite from Cerro Negro volcano (a-c) and laboratory experiments (d-f). The natroalunite often precipitates in close association with amorphous silica (si). Larger prismatic crystals in (d) are anhydrite, and "dg" is dried amorphous silica gel. Bright spots are spheroidal hematite. Images shown in (c) and (f) are from polished cross-sections of altered basalt cinders embedded in epoxy, while all others are from uncoated grains mounted on aluminum stubs. Arrows in (c), (d), and (f) point to psuedocubic crystals. In (c), the natroalunite is growing on amorphous silica, a common habitat in natural samples. Panel (f) shows cross-sections of larger psuedocubic crystals precipitated in gas vesicles from an altered basalt cinder. Crystals shown in panels (c) and (f) exhibit compositional zoning from darker, more Al-rich interiors to lighter, more Fe-rich exteriors. Cerro Negro images are from samples CN R20 and CN R21 (McCollom et al. 2013b) and laboratory images are from experiments ADSU5 and ADSU6 (McCollom et al. 2013a).

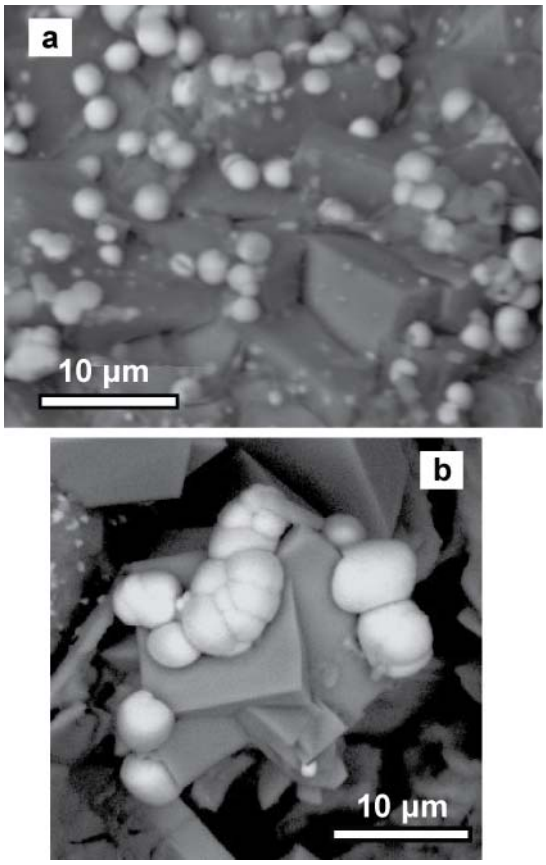

Figure 2. Examples of spheroidal hematite associated with Fe-bearing natroalunite in acid-sulfate altered rocks from (a) Cerro Negro and (b) basalt alteration experiments.

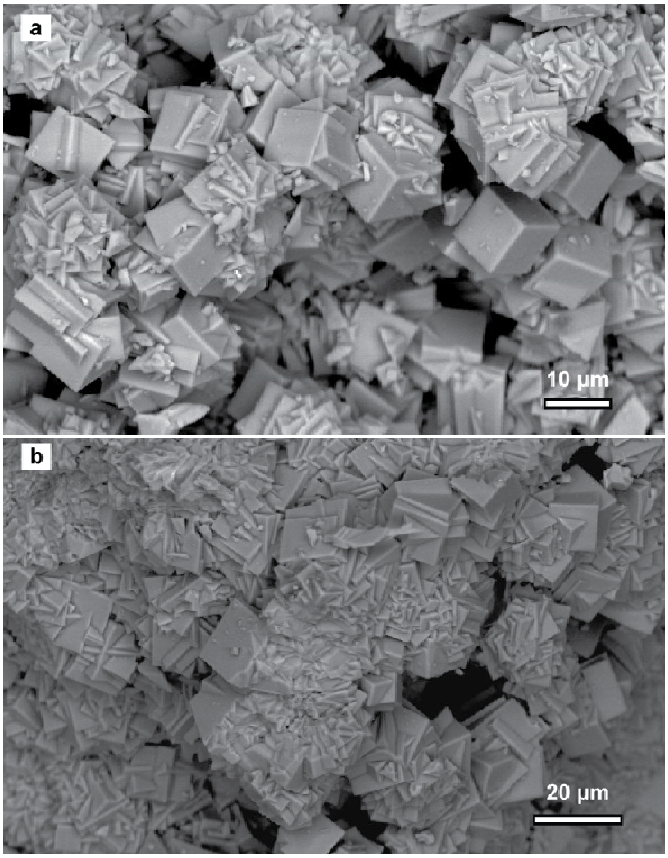

Figure 3. Backscattered electron images of synthetic natroalunite-natrojarosite solid solutions. (a) Natro3 (Fe#= 65). (b) Natro 4 (Fe#= 20).

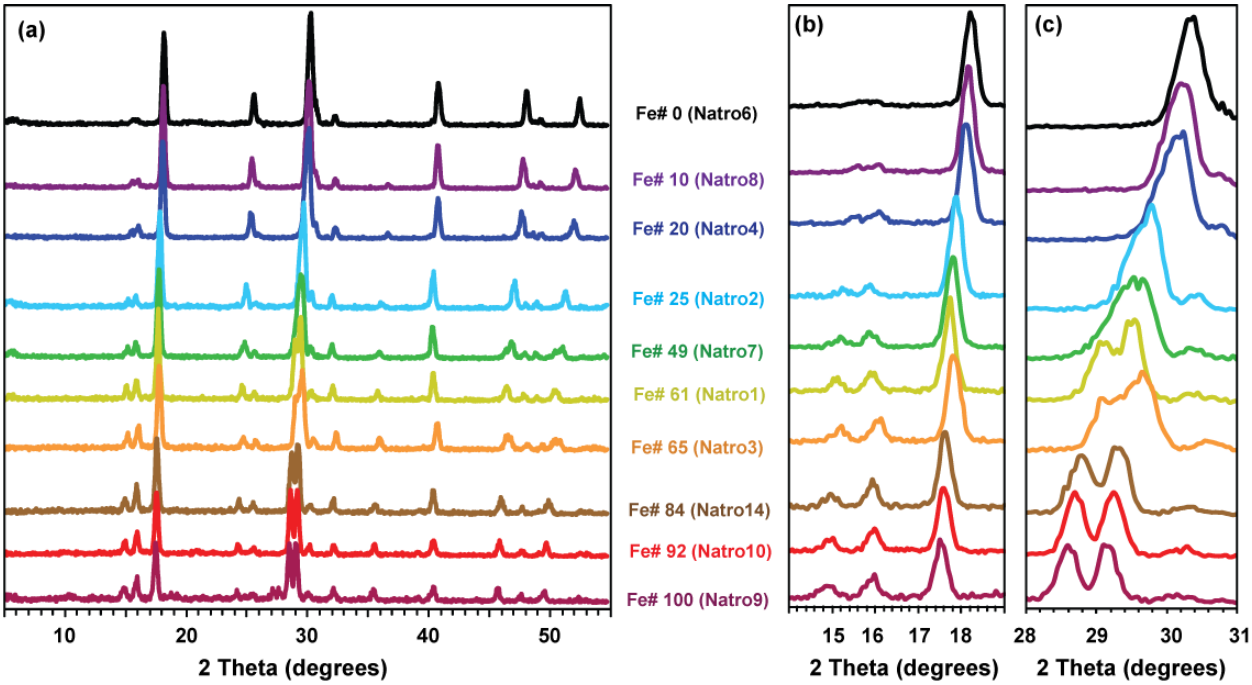

Figure 4. (a) X-ray diffractograms for synthetic natroalunite-natrojarosite solid solutions. (b,c) Expanded views of diffractograms for 2θ = 14-19° (b) and 28-31° (c).

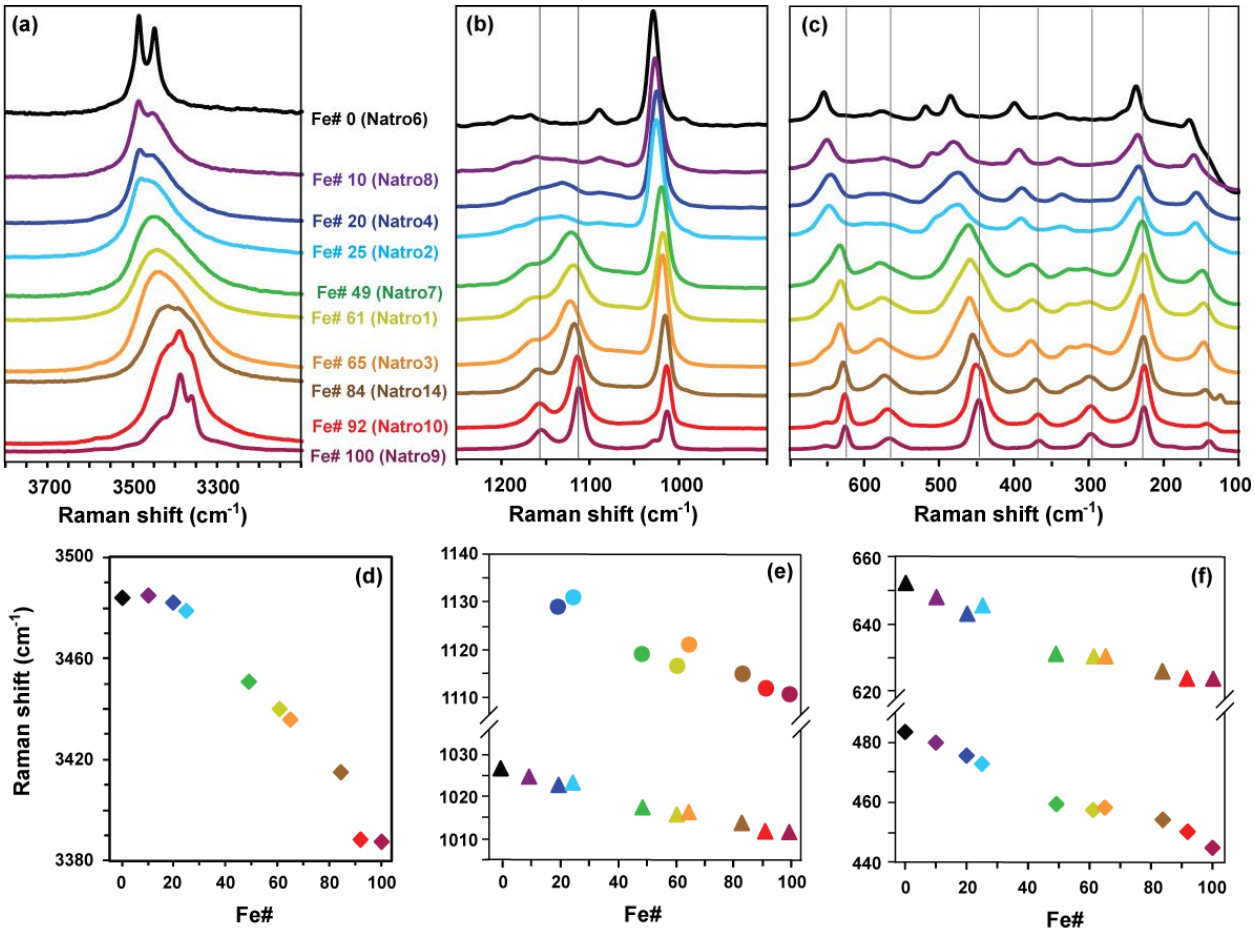

Figure 5. Raman analysis of synthetic natroalunite-natrojarosite solid solutions. (a,b,c) Raman peaks in the (a) OH/H_2O spectral range, (b) spectral range of SO_4^{2-} fundamental vibrations (ν_1 & ν_3), and (c) spectral range of fundamental vibrations (ν_2 & ν_4) and lattice modes. (d,e,f) Variations in Raman peak position with Fe content for selected peaks.

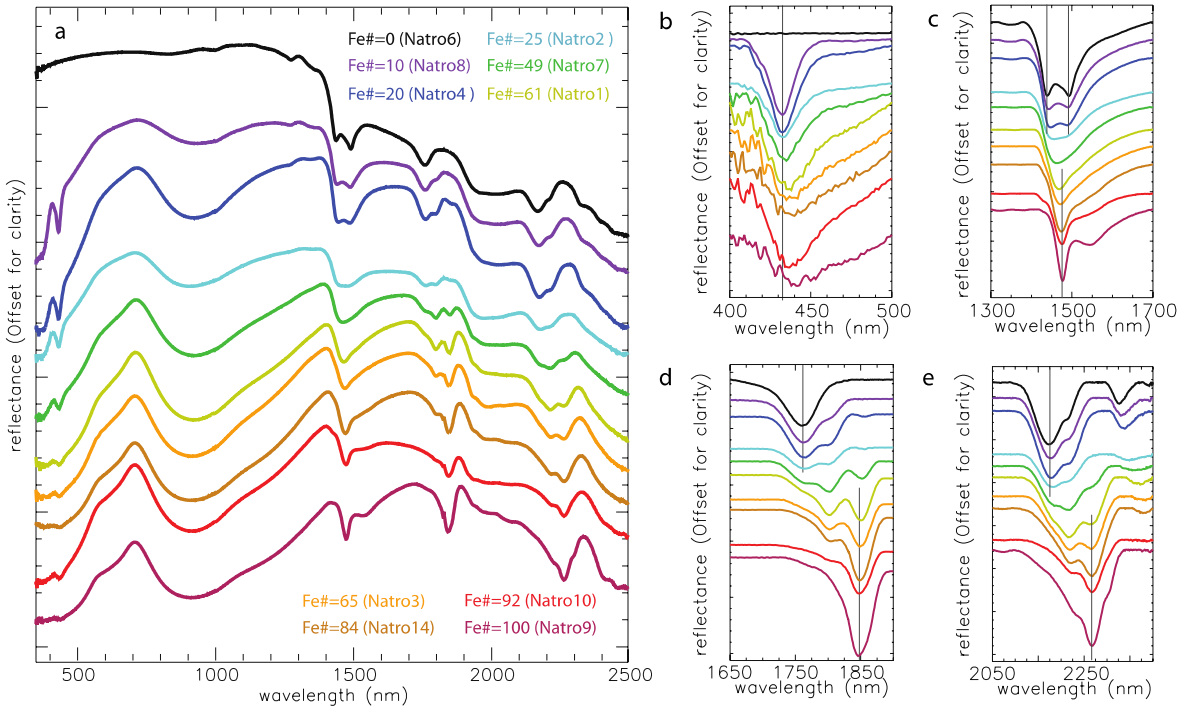

Figure 6. (a) Visible/near-infrared (VNIR) spectra of synthetic natroalunite-natrojarosite solid solutions. (b-e) Continuum removed data show systematic changes in absorption with Fe content for (b) a sharp electronic transition ($6A_{1g} \rightarrow {}^4T_{1g}$, $4E_g$) that is most prominent in intermediate Fe samples and for (c, d, e) combinations and overtones of OH-related bending and stretching vibrations which vary in position and intensity according to iron content, with the sample of higher Fe contents generally having absorption centers at longer wavelength.

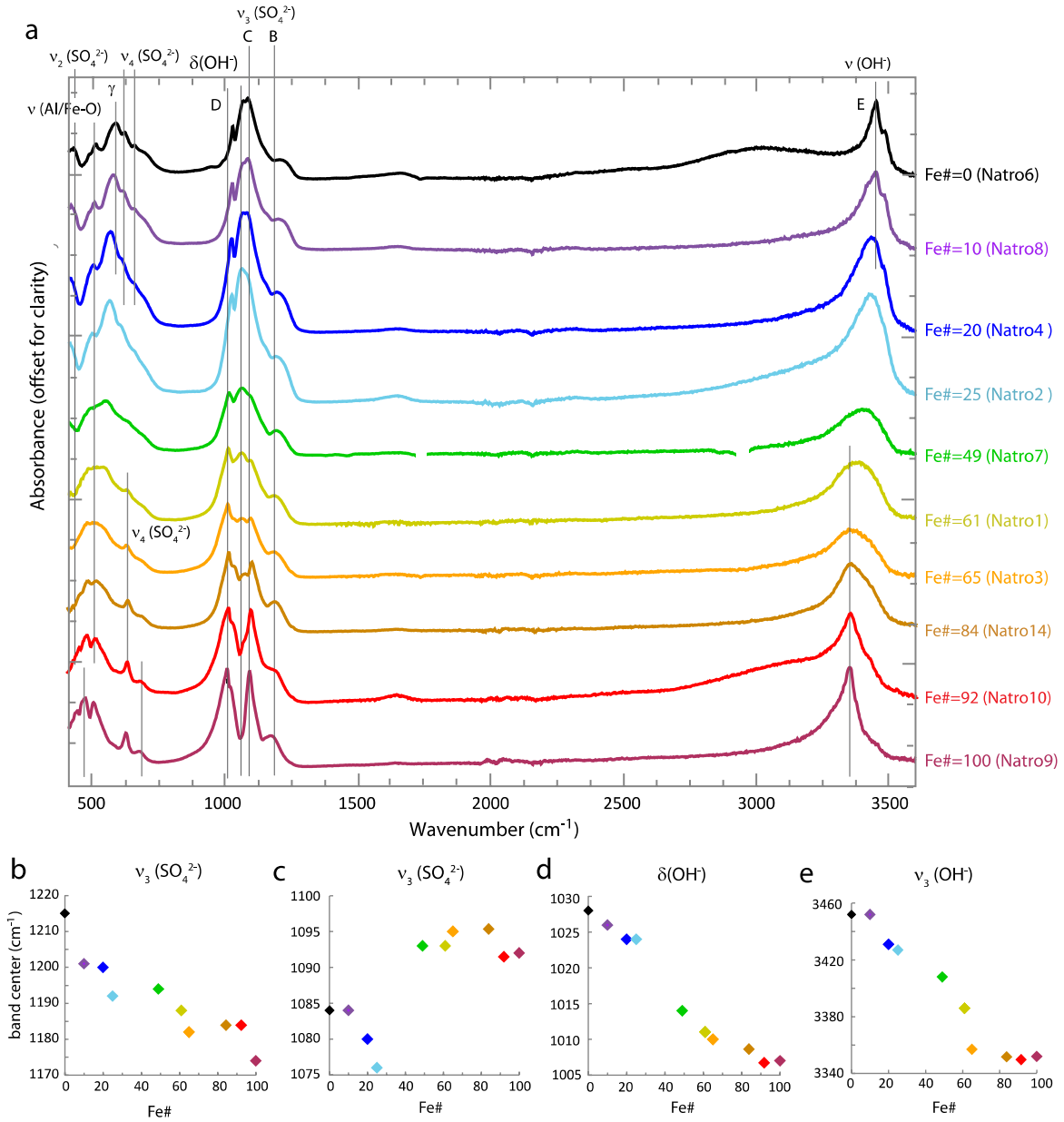

Figure 7. (a) Attenuated total reflectance (ATR) Mid-IR spectra of synthetic natroalunite-natrojarosite solid solutions. (b-e) Plots of band center versus iron content of the sample (Fe#) indicate, depending on the band in question, systematic or gradual changes in the positions of the strongest absorptions due to (b,c) ν_3 (SO_4^{2-}), (d) δ (OH) ,and (e) ν_3 (OH), that correlate with changes in iron content. In general, band centers shift to lower wavenumbers (longer wavelengths) with increasing Fe# though some band centers (e.g. panels c, e) appear to instead have discrete positions depending on whether the natroalunite structure is relatively Al- or Fe-enriched.

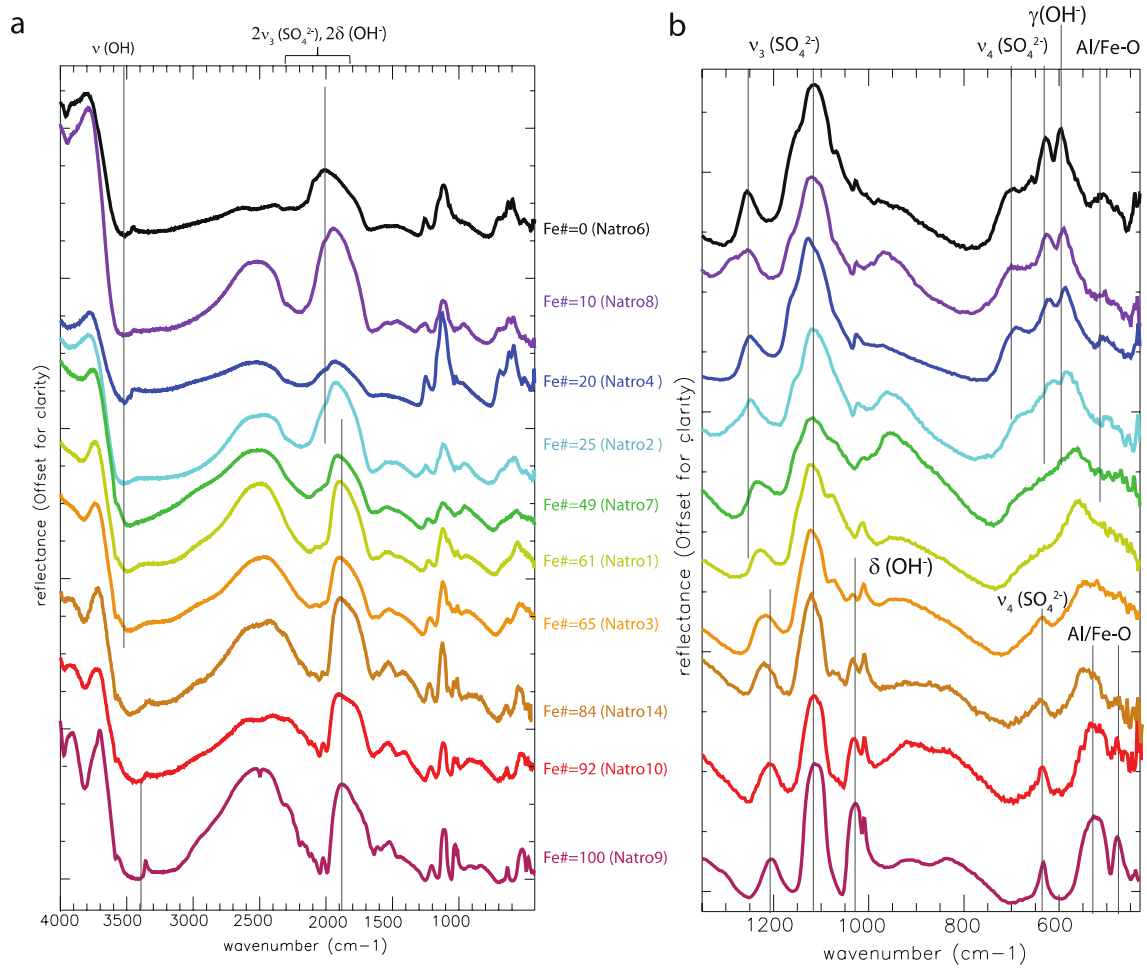

Figure 8. (a) Mid-infrared diffuse reflectance spectra of synthetic natroalunite-natrojarosite solid solutions. (b) Expanded view of 430-1350 cm^{-1}. Attributions of vibrational absorptions are discussed in text.

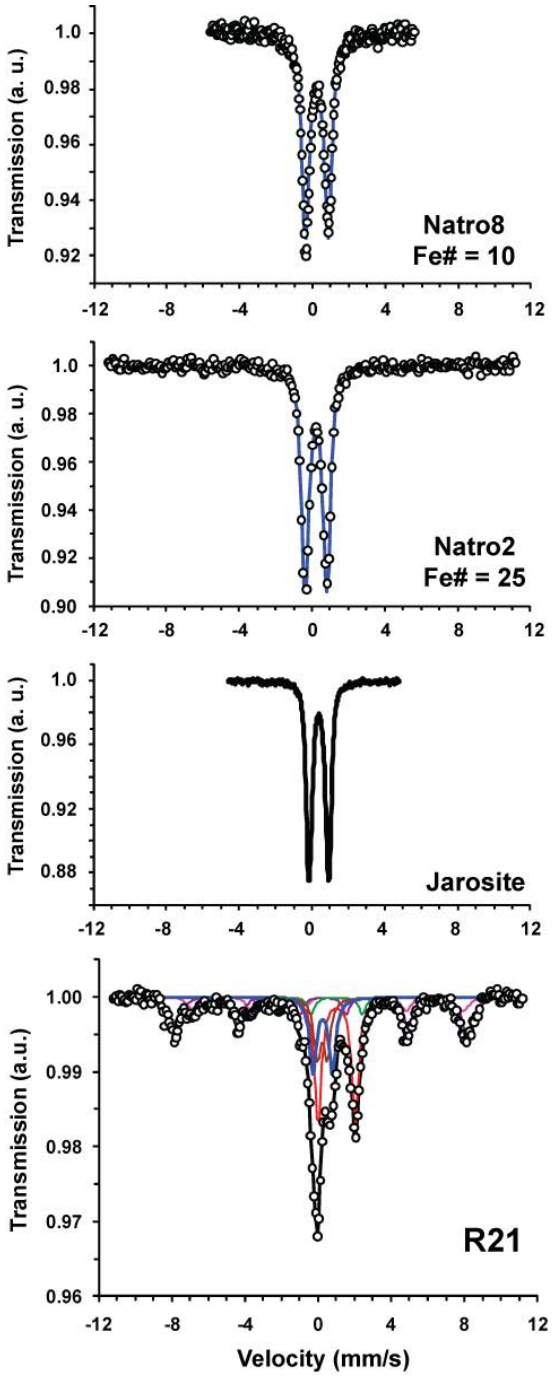

Figure 9. Mössbauer spectra for synthetic natroalunite with Fe# = 10 (Natro8) and Fe# = 25 (Natro2), a library spectrum for jarosite (RRUFF database), and an example of acid-sulfate altered basalt from Cerro Negro (CN R21). Black circles are measured values. Synthetic natroalunite samples are fit with a single component (blue line). For the CN sample, the black line represents the total fit to the data using the components shown by colored lines, including minerals from the alunite group (blue), augite (red, aqua), olivine (green), Fe-oxide/oxyhydroxide (brown) and titanomagnetite (purple, pink).

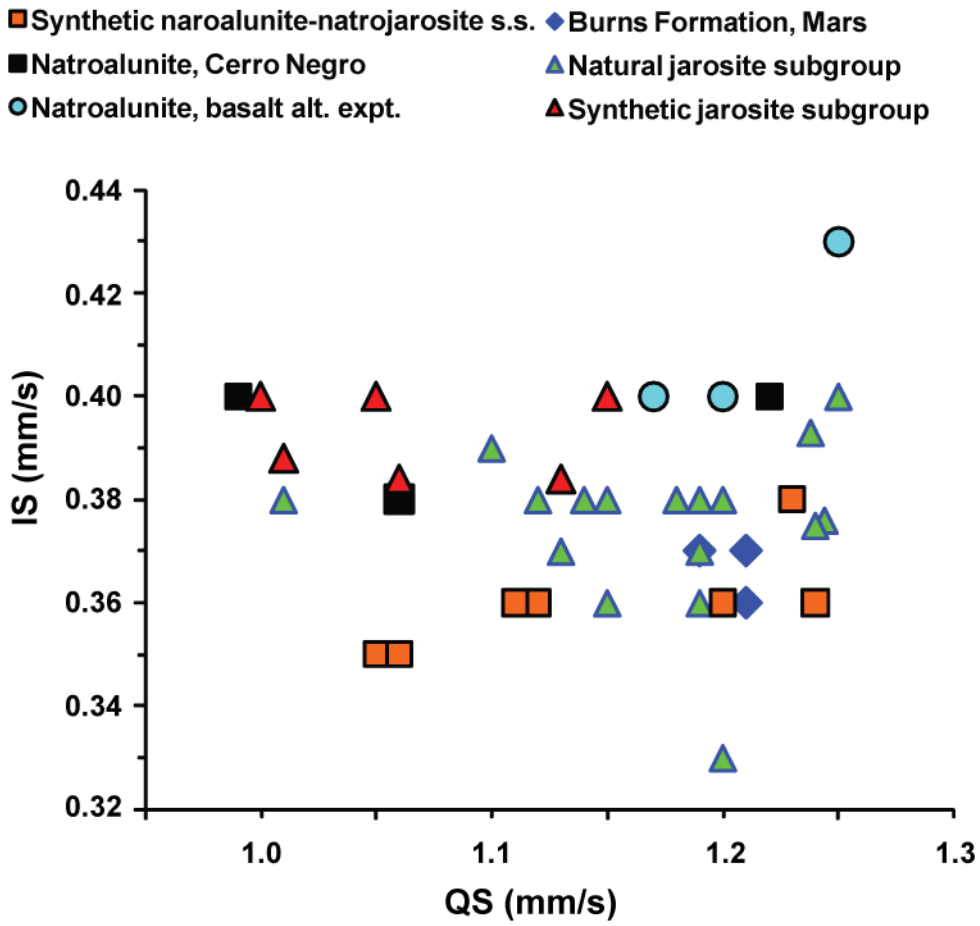

Figure 10. Mössbauer parameters (isomer shift, IS, versus quadrapole splitting, QS) for synthetic natroalunite-natrojarosite solid solutions, for the alunite group component in acid-sulfate altered basalt cinders at Cerro Negro, and for Fe-bearing natroalunite produced during experimental simulation of basalt acid-sulfate alteration. Included for comparison are some published parameters for natural and synthetic members of the jarosite subgroup and for the Fe3D4 phase from Meridiani Planum on Mars interpreted to be jarosite (data from Morris et al. 2006, and references therein). Data for Cerro Negro and basalt alteration experiments are from McCollom et al. (2013a,b).

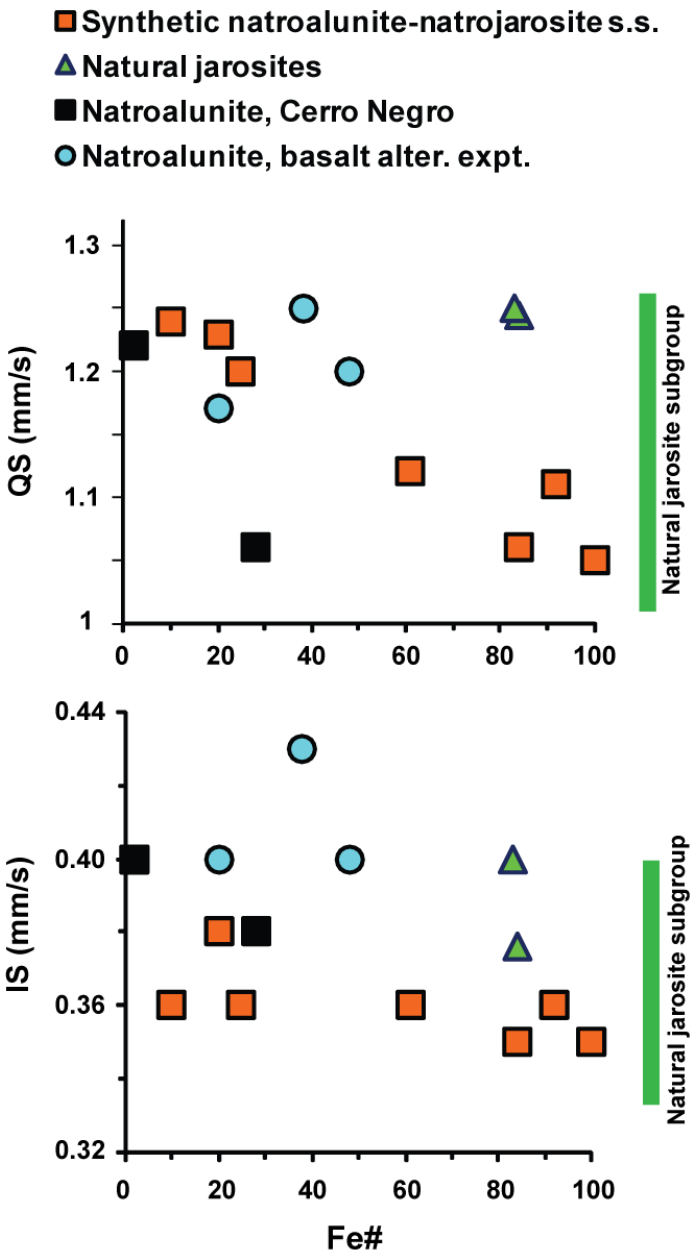

Figure 11. Variation in Mössbauer parameters quadrapole splitting (QS) and isomer shift (IS) as a function of Fe content of alunite group minerals, expressed as Fe#. Green bars define range of values for natural minerals from the jarosite subgroup compiled by Morris et al. (2006). Data for Al-bearing natrojarosites from Hrynkiewicz et al. (1965) and Johnson (1977), and for Cerro Negro and basalt alteration experiments from McCollom et al. (2013a,b).

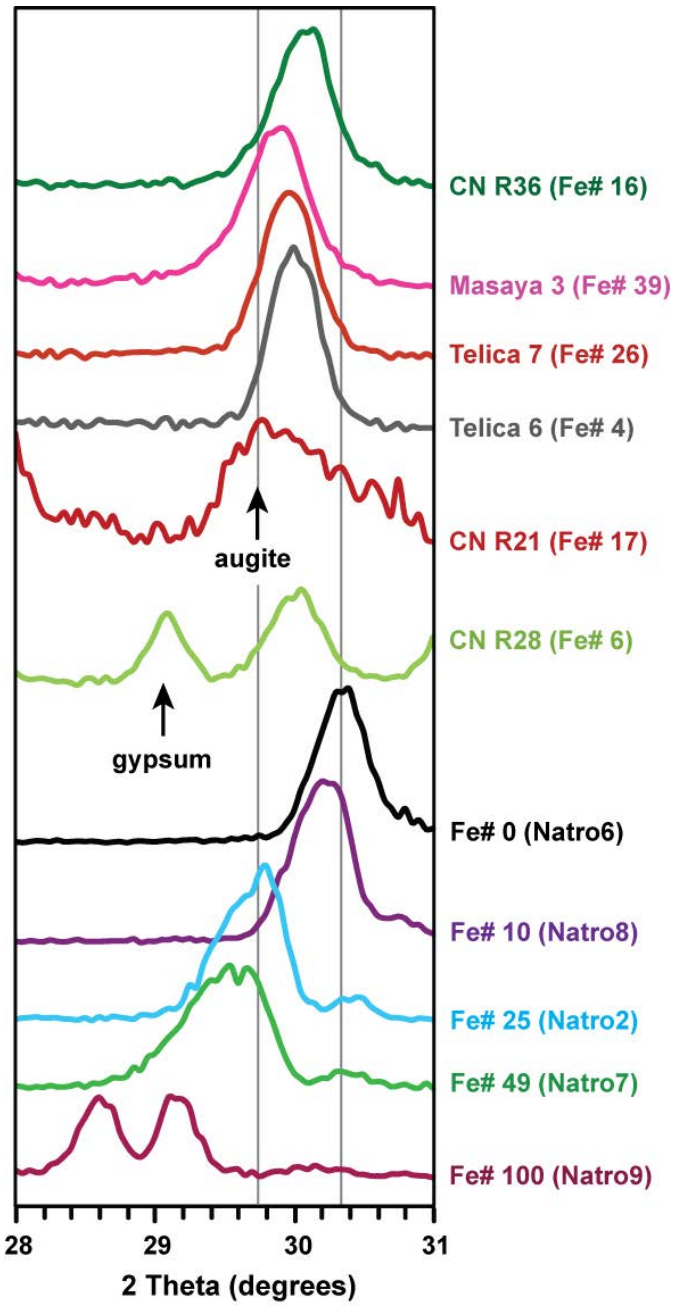

Figure 12. Partial X-ray diffractograms for acid-sulfate altered deposits from Cerro Negro, Telica, and Masaya volcanoes. The figure shows peaks between 2Θ = 28 and 31°, encompassing the range where primary diffraction peaks for natroalunite-natrojarosite solid solutions occur.

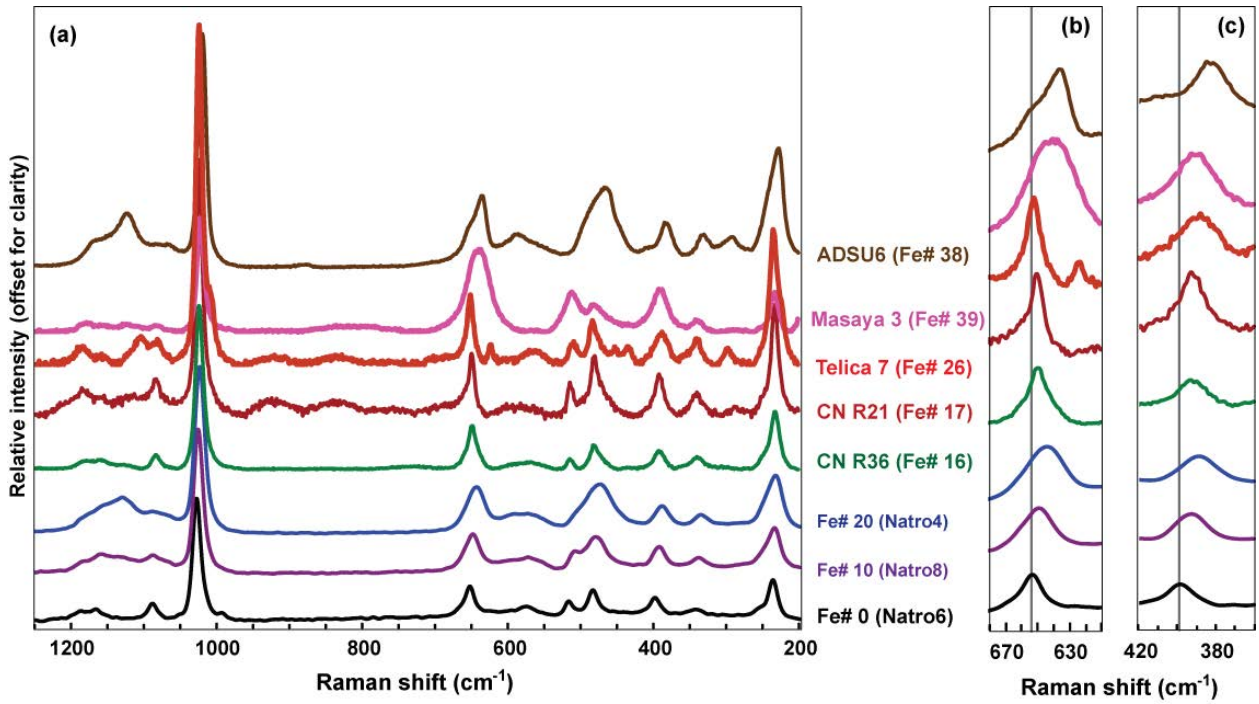

Figure 13. (a) Raman spectra of individual crystals in natural samples from Cerro Negro (CN R21, CN R36) and from a laboratory experiment (ADSU6). Shown for comparison are several spectra from the synthetic natroalunites. (b,c) Expanded views of spectra at Raman shifts in the ranges 680-610 cm^{-1} (b) and 540-420 cm^{-1} (c).

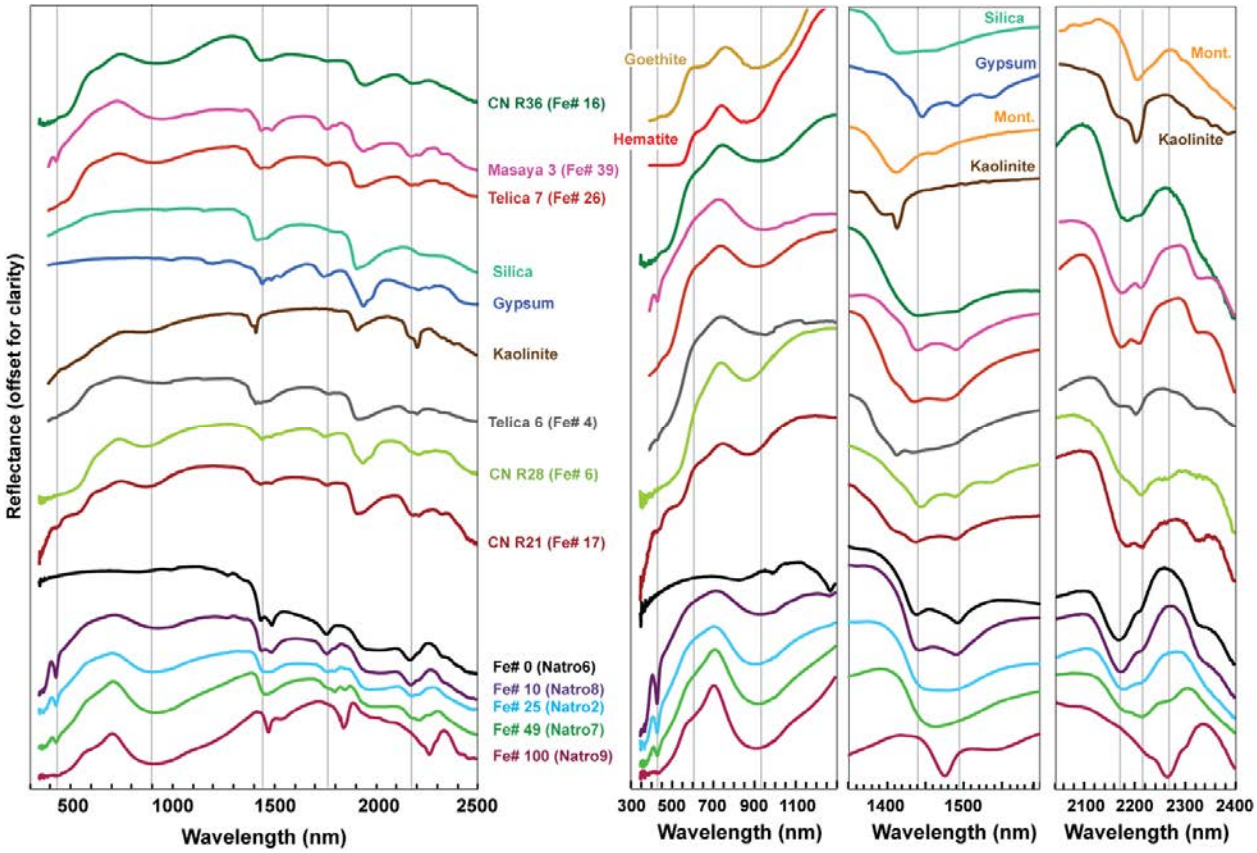

Figure 14. VNIR spectra of natural samples from Cerro Negro, Telica, and Masaya volcanoes. Samples Telica 7, Telica 6, and Masaya 3 measured in the field (Marcucci et al. 2013), other spectra measured in the laboratory. Mont. = montmorillonite.

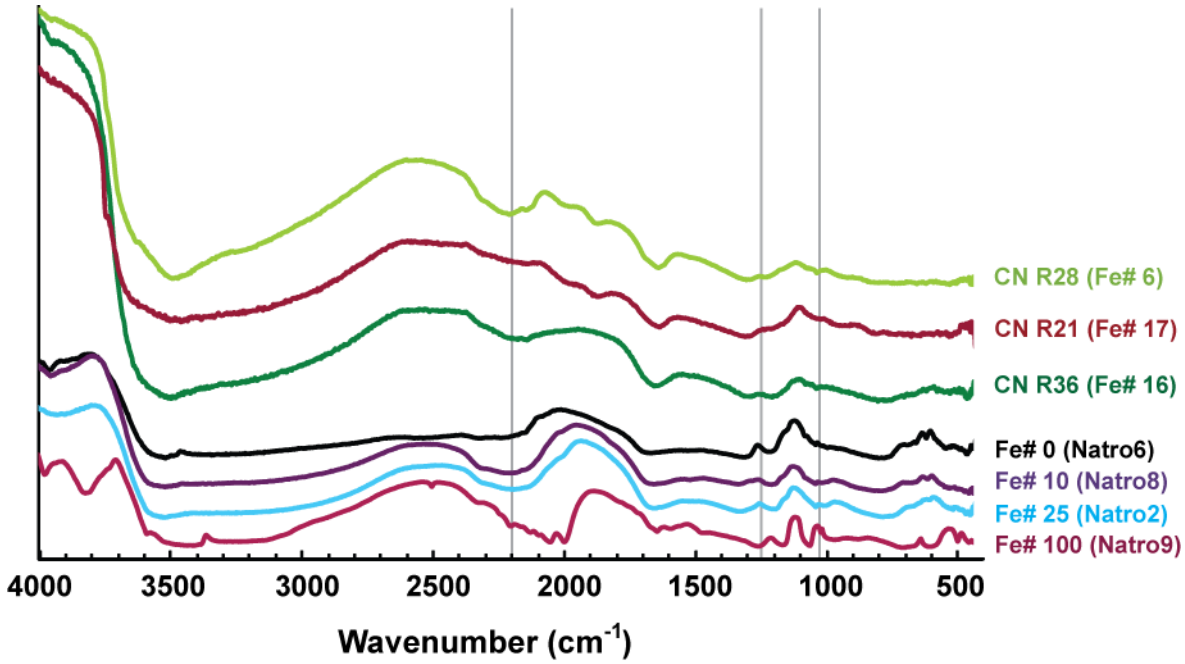

Figure 15. Mid-infrared diffuse reflectance spectra of natural samples from Cerro Negro, with several spectra from synthetic minerals shown for reference.

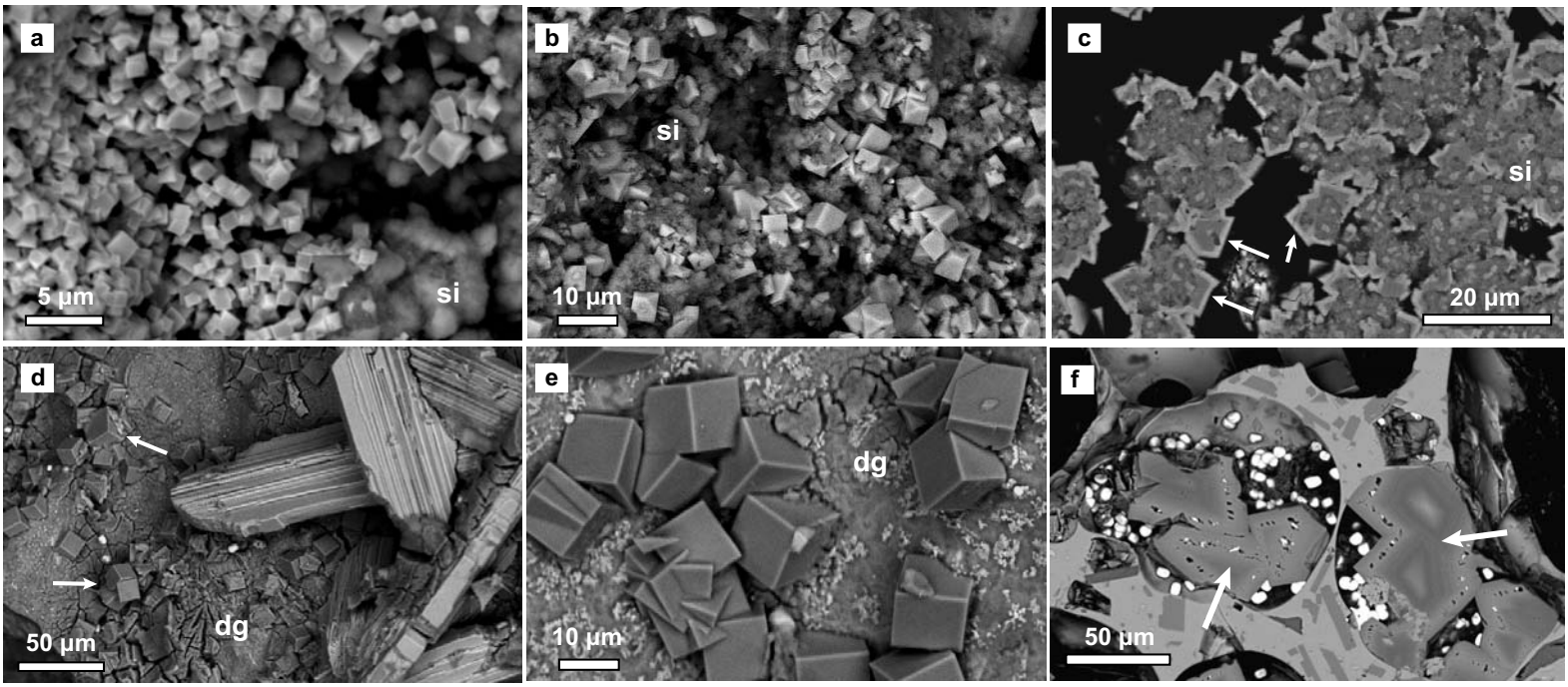
a
5 µm
si
b
si
10 µm
c
si
20 µm
d
dg
50 µm
e
dg
10 µm
f
50 µm

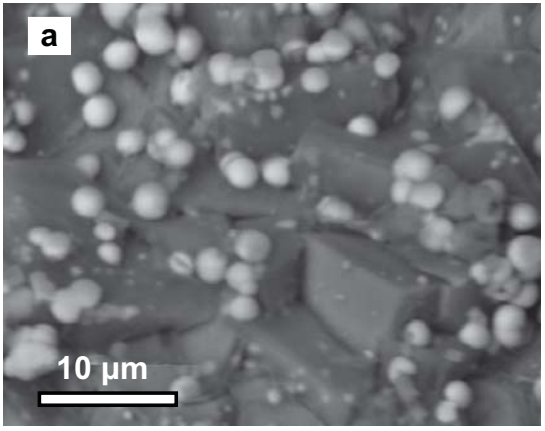
a
10 µm

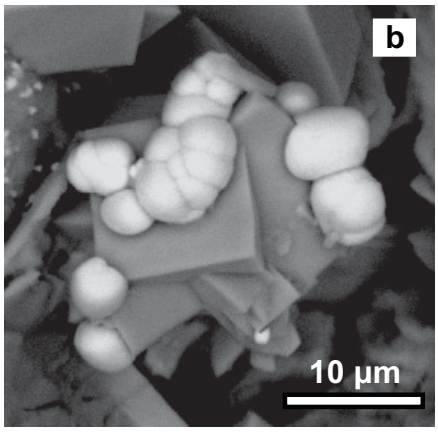
b
10 µm

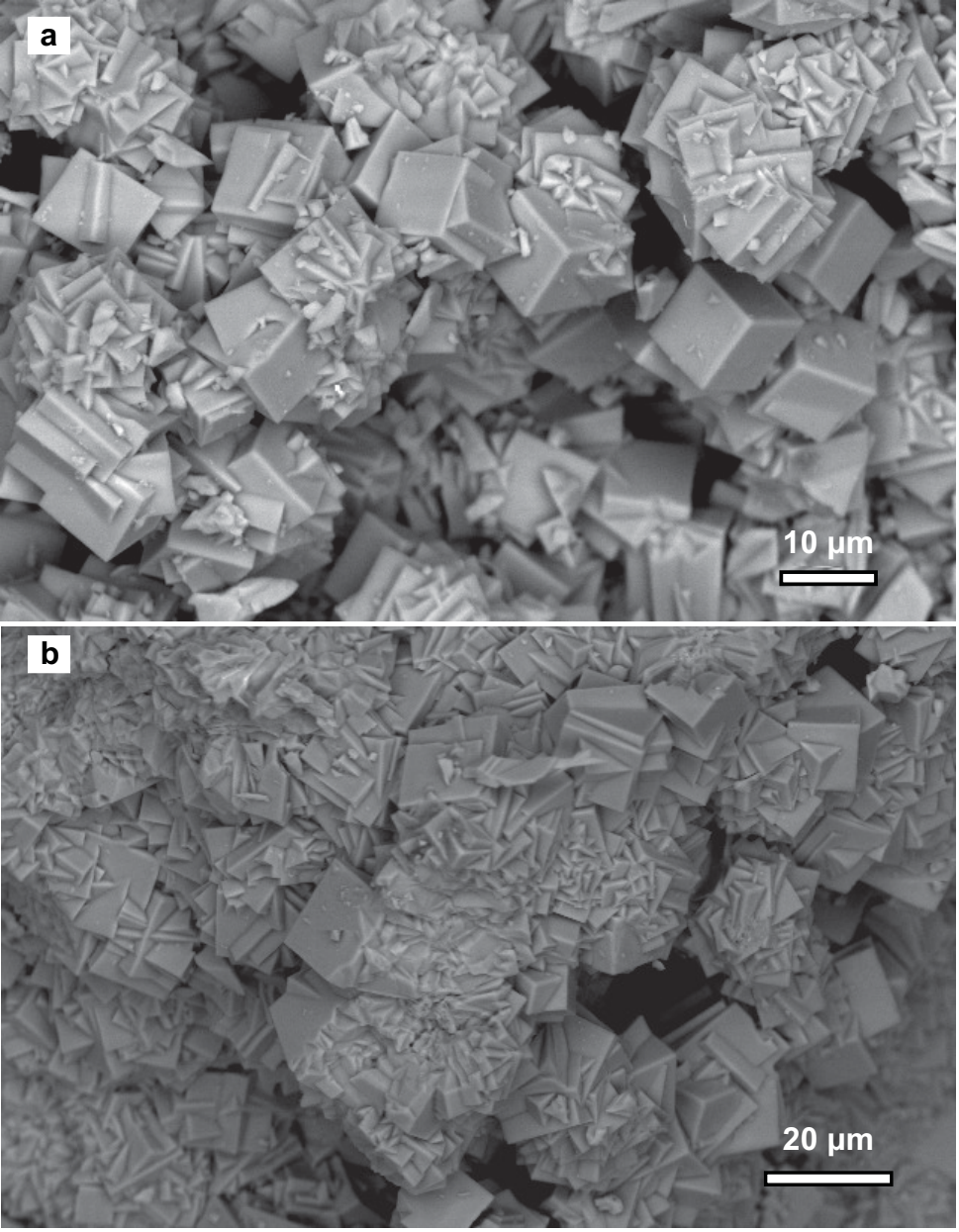
a
10 µm
b
20 µm

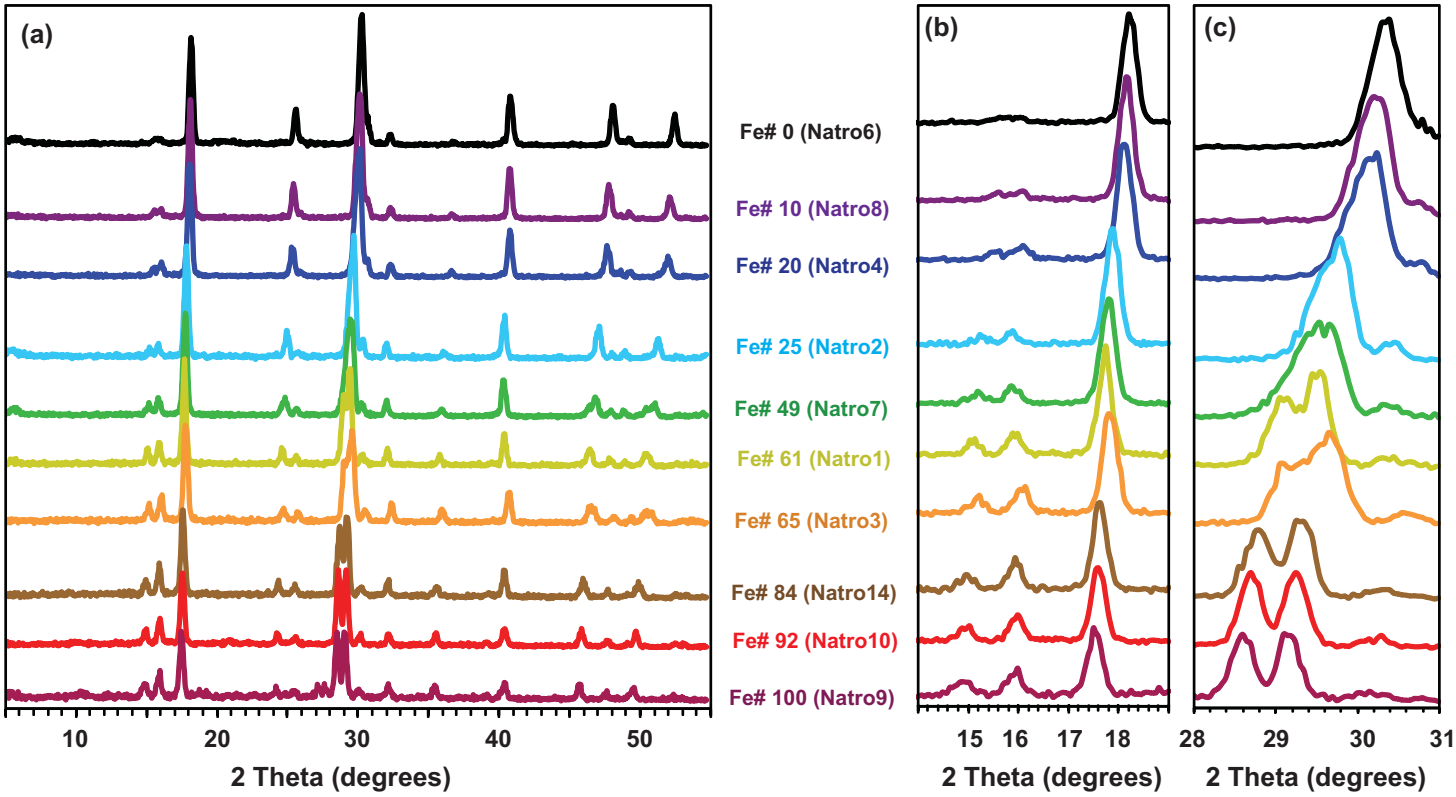
(a)
(b)
(c)
Fe# 0 (Natro6)
Fe# 10 (Natro8)
Fe# 20 (Natro4)
Fe# 25 (Natro2)
Fe# 49 (Natro7)
Fe# 61 (Natro1)
Fe# 65 (Natro3)
Fe# 84 (Natro14)
Fe# 92 (Natro10)
Fe# 100 (Natro9)
10
20
30
40
50
15
16
17
18
28
29
30
31
2 Theta (degrees)
2 Theta (degrees)
2 Theta (degrees)

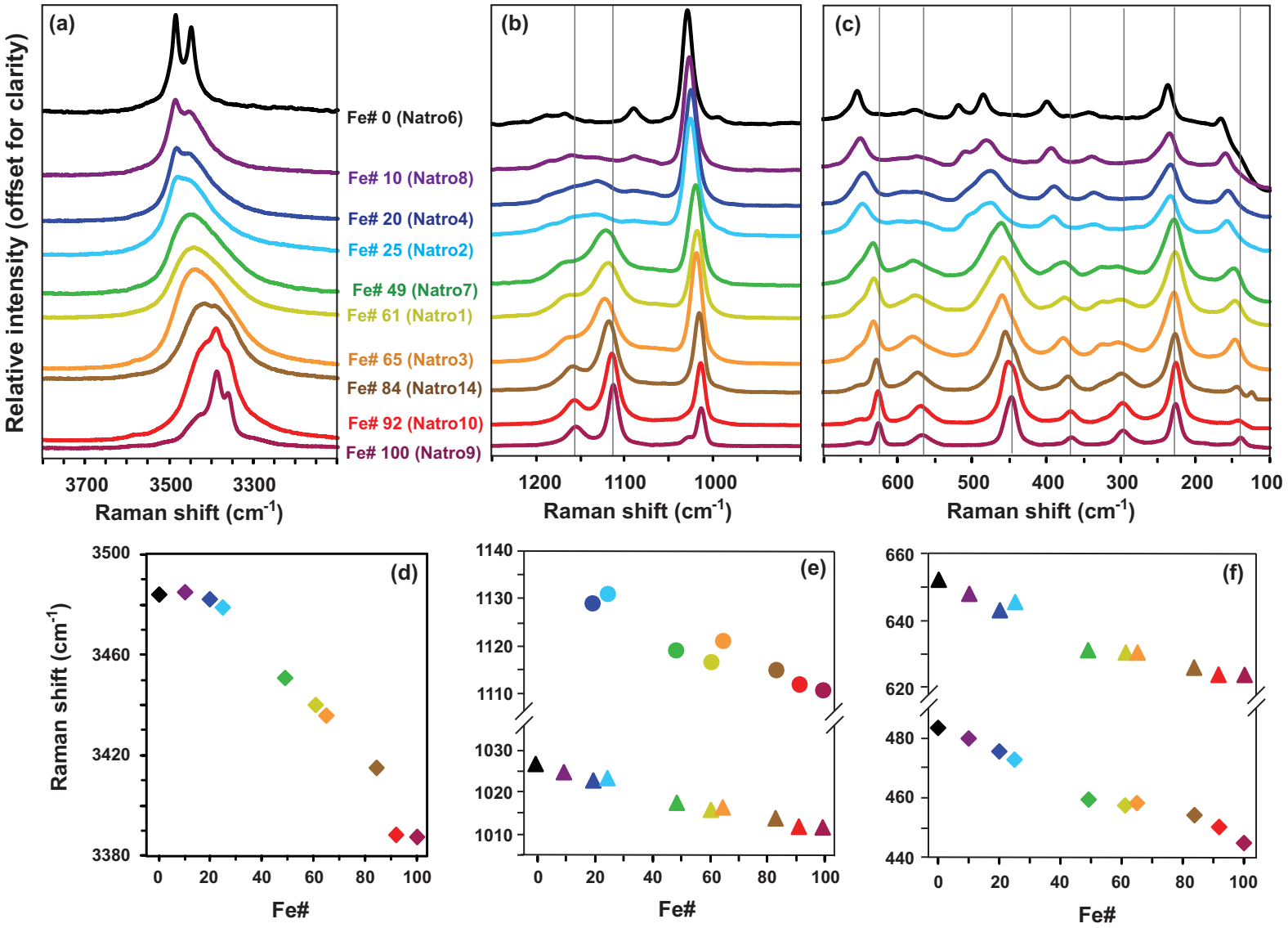
(a)
(b)
(c)
Relative intensity (offset for clarity)
Fe# 0 (Natro6)
Fe# 10 (Natro8)
Fe# 20 (Natro4)
Fe# 25 (Natro2)
Fe# 49 (Natro7)
Fe# 61 (Natro1)
Fe# 65 (Natro3)
Fe# 84 (Natro14)
Fe# 92 (Natro10)
Fe# 100 (Natro9)
3700 3500 3300
1200 1100 1000
600 500 400 300 200 100
Raman shift (cm-1)
(d)
(e)
(f)
Raman shift (cm-1)
3500 3460 3420 3380
1140 1130 1120 1110 1030 1020 1010
660 640 620 480 460 440
0 20 40 60 80 100
Fe#

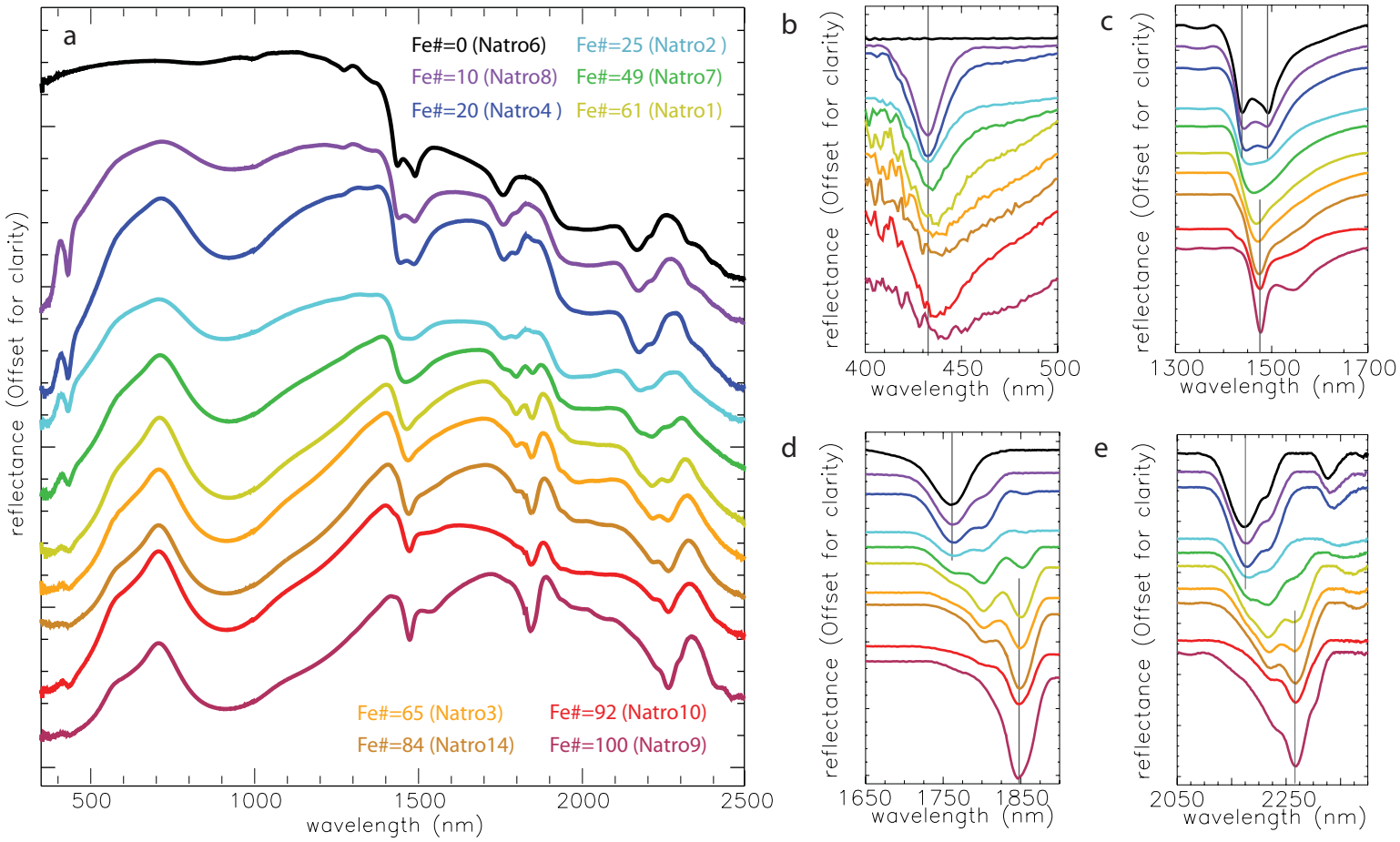
a
Fe#=0 (Natro6)
Fe#=25 (Natro2)
Fe#=10 (Natro8)
Fe#=49 (Natro7)
Fe#=20 (Natro4)
Fe#=61 (Natro1)
Fe#=65 (Natro3)
Fe#=92 (Natro10)
Fe#=84 (Natro14)
Fe#=100 (Natro9)
reflectance (Offset for clarity)
wavelength (nm)
500
1000
1500
2000
2500
b
c
d
e
400
450
500
1300
1500
1700
1650
1750
1850
2050
2250

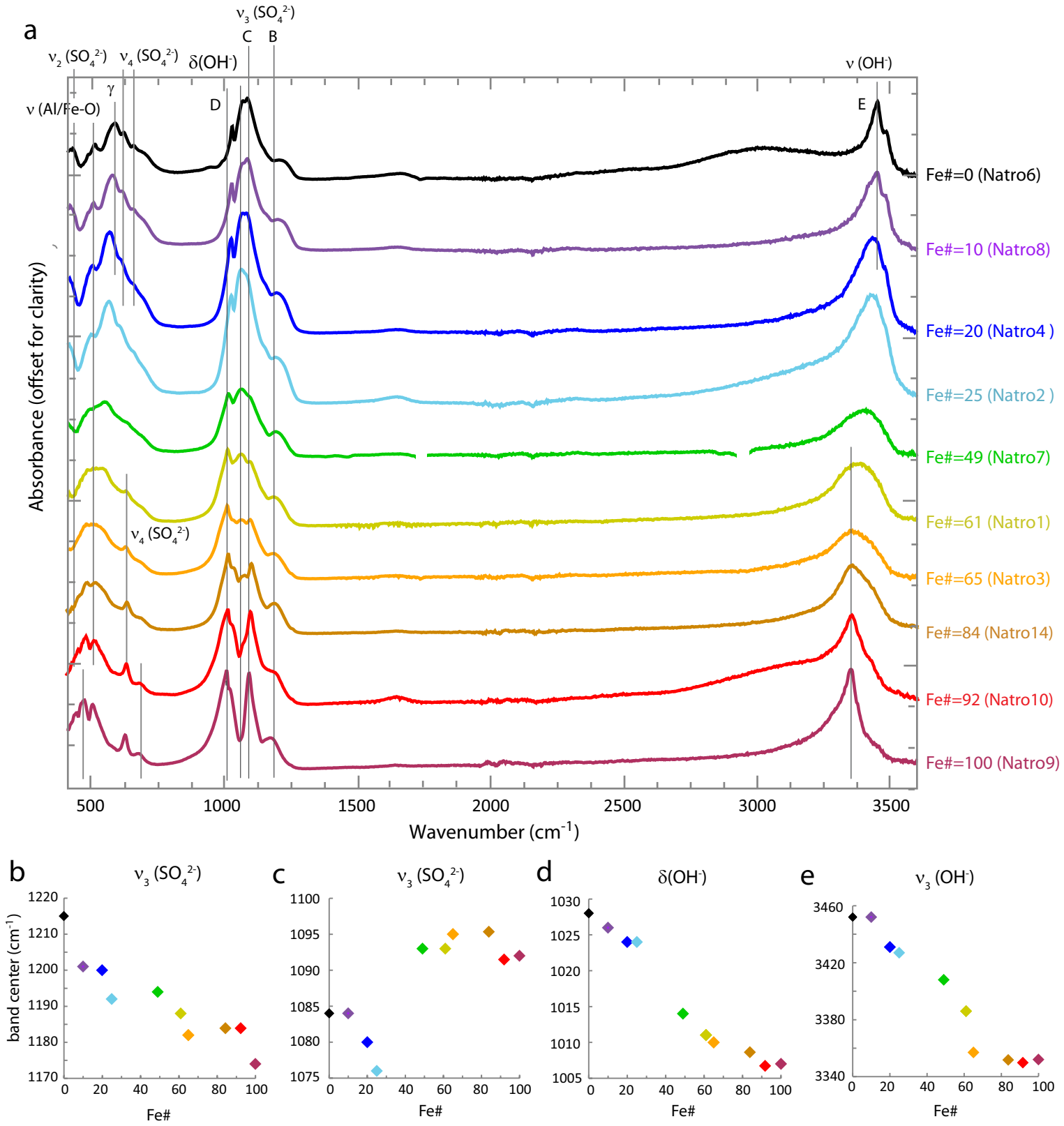
a
ν3 (SO4 2-)
C
B
ν2 (SO4 2-)
ν4 (SO4 2-)
δ(OH-)
ν (OH-)
γ
ν (Al/Fe-O)
D
E
Fe#=0 (Natro6)
Fe#=10 (Natro8)
Fe#=20 (Natro4)
Fe#=25 (Natro2)
Fe#=49 (Natro7)
Fe#=61 (Natro1)
Fe#=65 (Natro3)
Fe#=84 (Natro14)
Fe#=92 (Natro10)
Fe#=100 (Natro9)
ν4 (SO4 2-)
Absorbance (offset for clarity)
500
1000
1500
2000
2500
3000
3500
Wavenumber (cm-1)
b
ν3 (SO4 2-)
band center (cm-1)
1220
1210
1200
1190
1180
1170
0
20
40
60
80
100
Fe#
c
ν3 (SO4 2-)
1100
1095
1090
1085
1080
1075
Fe#
d
δ(OH-)
1030
1025
1020
1015
1010
1005
Fe#
e
ν3 (OH-)
3460
3420
3380
3340
Fe#

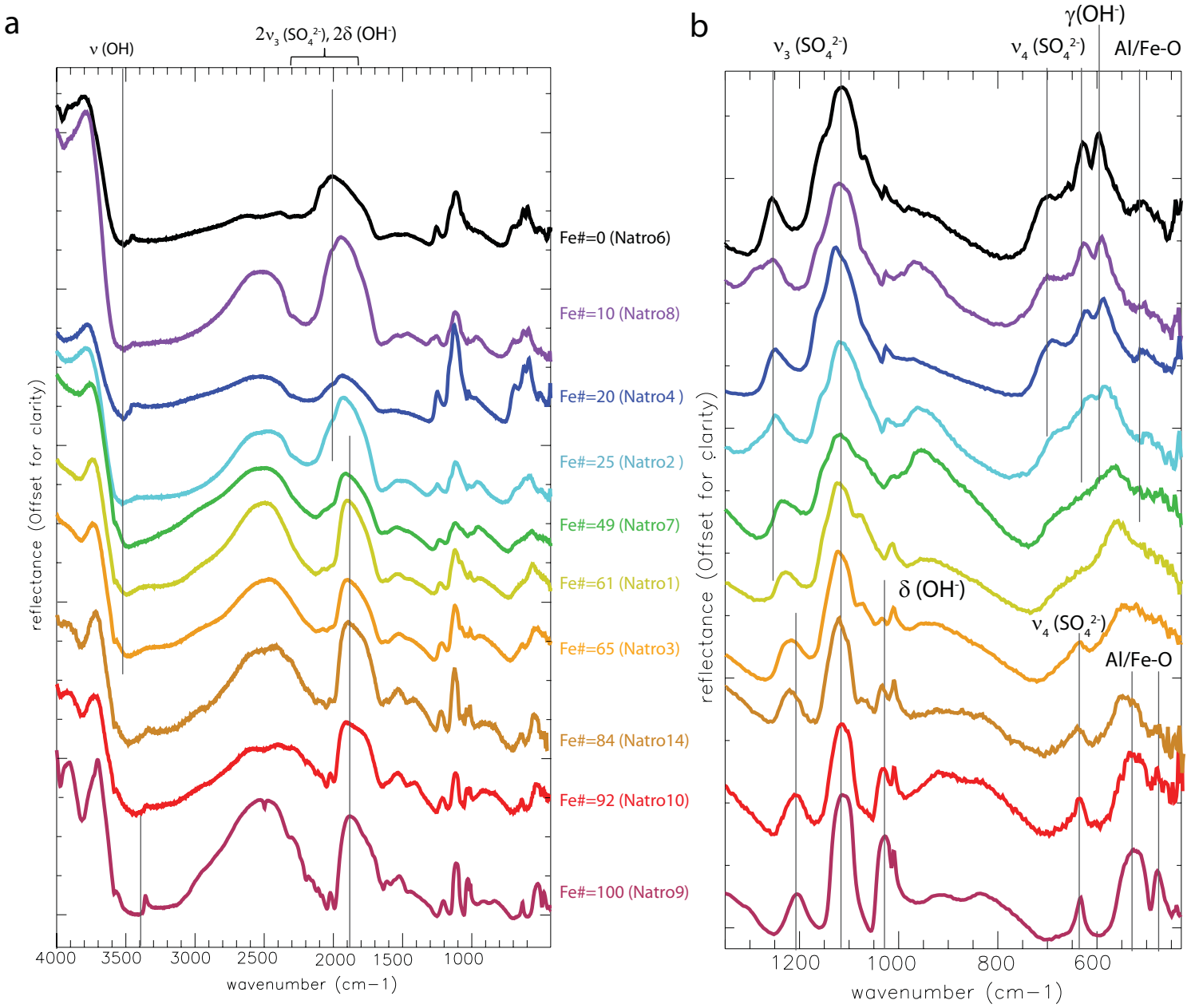
a
ν (OH)
2ν3 (SO4 2-), 2δ (OH-)
Fe#=0 (Natro6)
Fe#=10 (Natro8)
Fe#=20 (Natro4)
Fe#=25 (Natro2)
Fe#=49 (Natro7)
Fe#=61 (Natro1)
Fe#=65 (Natro3)
Fe#=84 (Natro14)
Fe#=92 (Natro10)
Fe#=100 (Natro9)
reflectance (Offset for clarity)
4000 3500 3000 2500 2000 1500 1000
wavenumber (cm−1)
b
ν3 (SO4 2-)
ν4 (SO4 2-)
γ(OH-)
Al/Fe-O
δ (OH-)
ν4 (SO4 2-)
Al/Fe-O
reflectance (Offset for clarity)
1200 1000 800 600
wavenumber (cm−1)

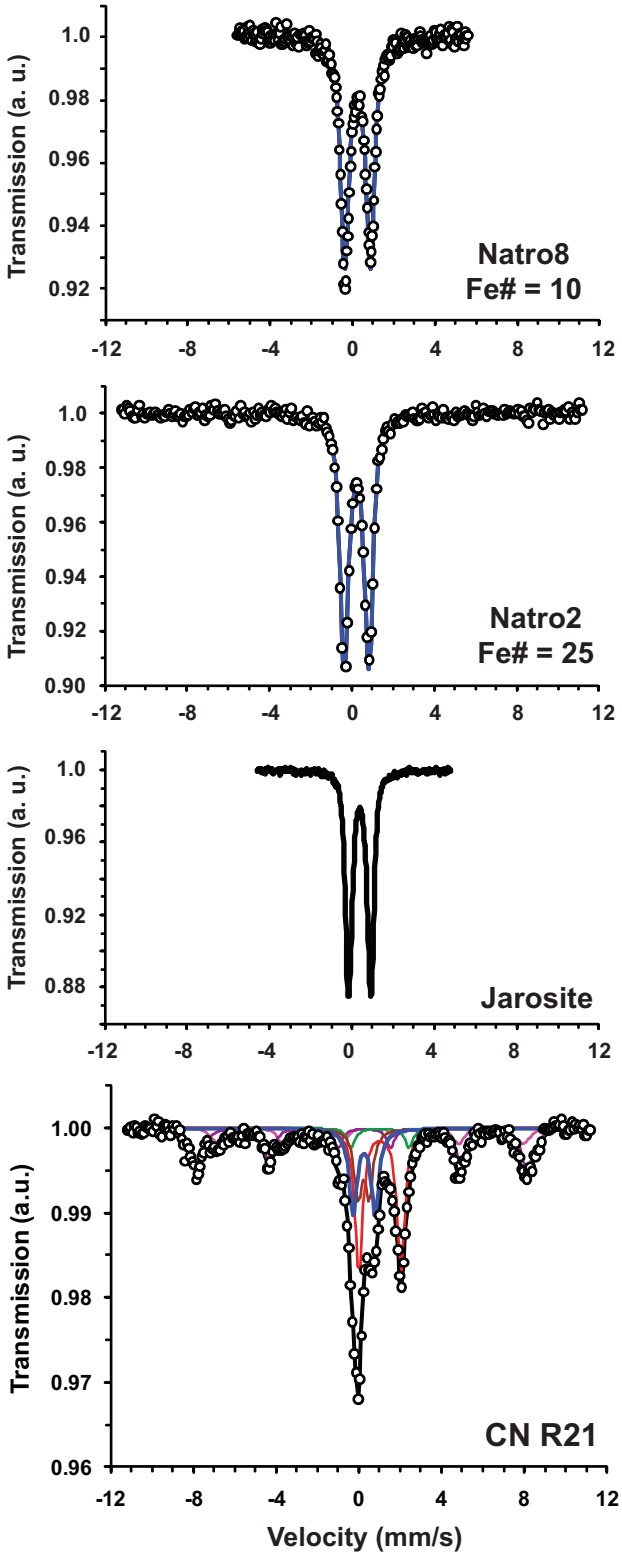
Transmission (a. u.)
1.0
0.98
0.96
0.94
0.92
Natro8
Fe# = 10
-12
-8
-4
0
4
8
12
Transmission (a. u.)
1.0
0.98
0.96
0.94
0.92
0.90
Natro2
Fe# = 25
-12
-8
-4
0
4
8
12
Transmission (a. u.)
1.0
0.96
0.92
0.88
Jarosite
-12
-8
-4
0
4
8
12
Transmission (a.u.)
1.00
0.99
0.98
0.97
0.96
CN R21
-12
-8
-4
0
4
8
12
Velocity (mm/s)

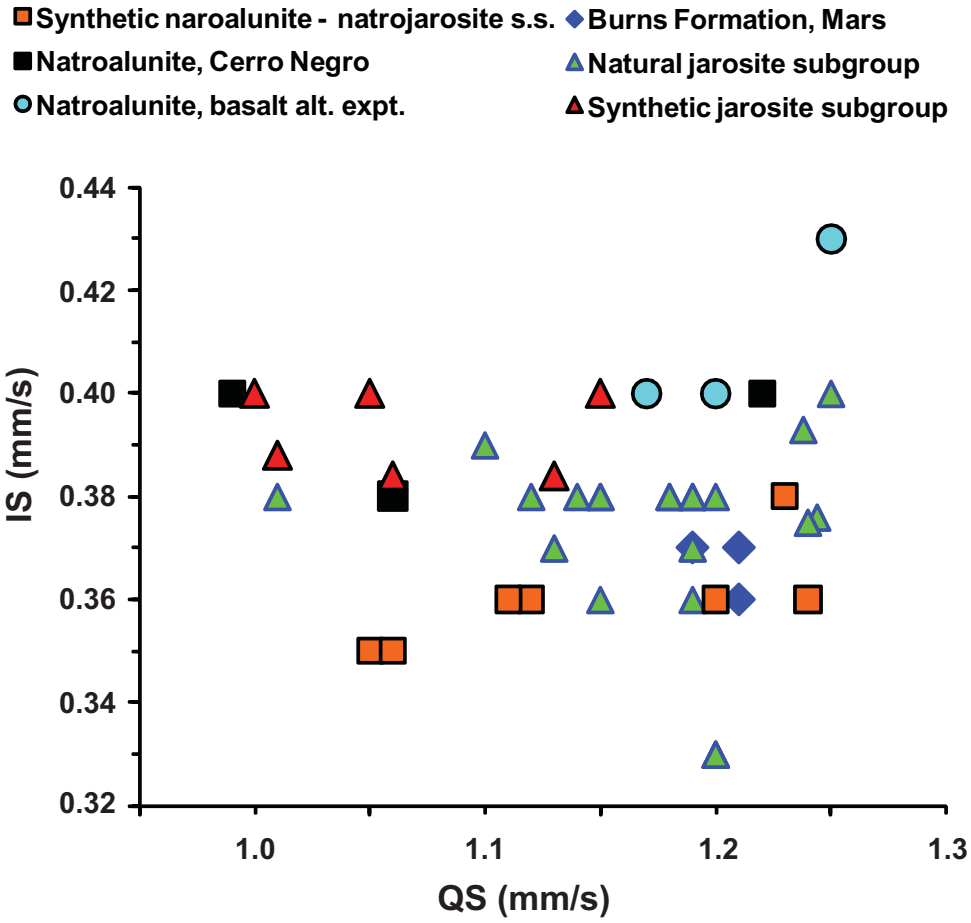
Synthetic naroalunite - natrojarosite s.s.
Burns Formation, Mars
Natroalunite, Cerro Negro
Natural jarosite subgroup
Natroalunite, basalt alt. expt.
Synthetic jarosite subgroup
IS (mm/s)
0.44
0.42
0.40
0.38
0.36
0.34
0.32
1.0
1.1
1.2
1.3
QS (mm/s)

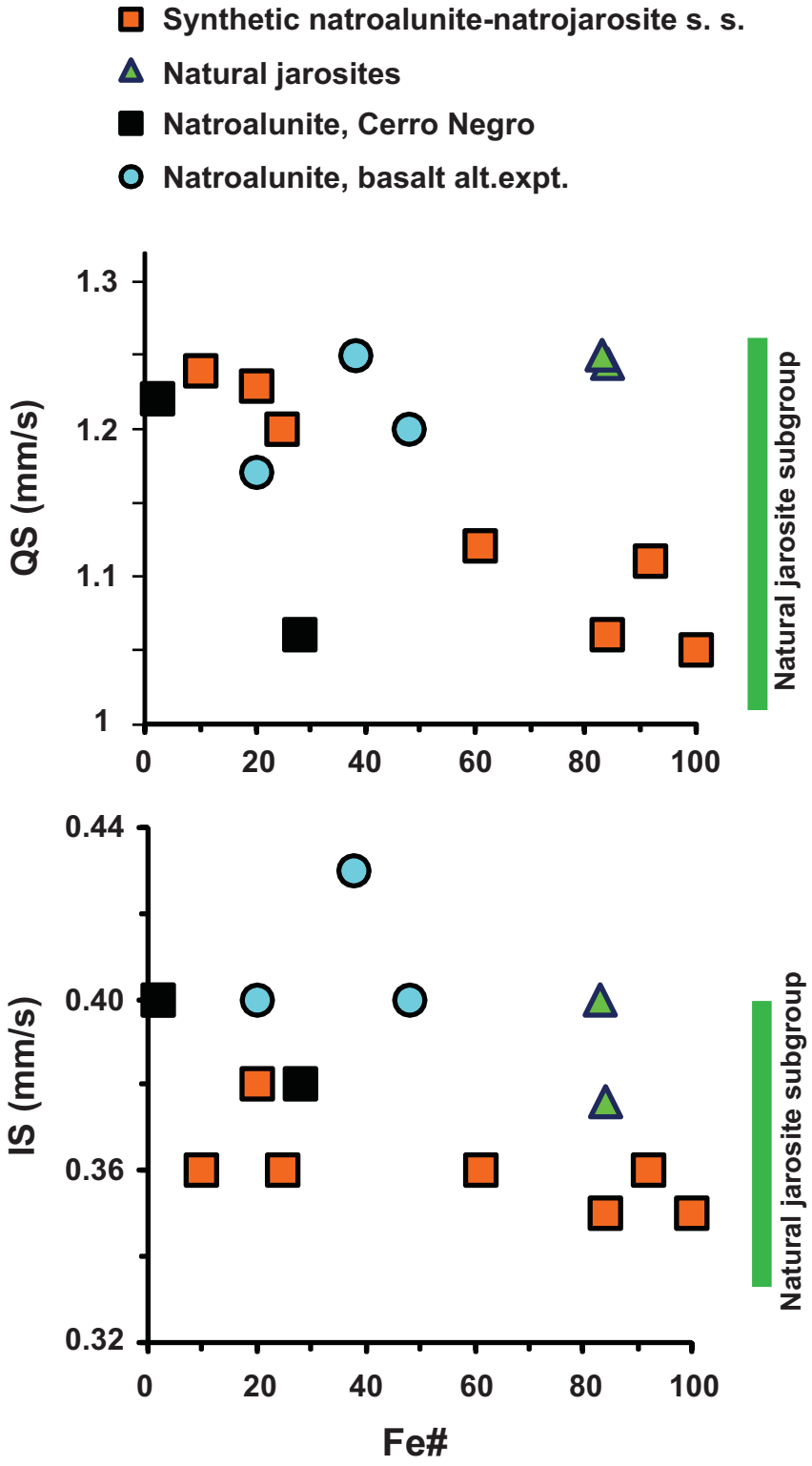
Synthetic natroalunite-natrojarosite s. s.
Natural jarosites
Natroalunite, Cerro Negro
Natroalunite, basalt alt.expt.
QS (mm/s)
1.3
1.2
1.1
1
0
20
40
60
80
100
Natural jarosite subgroup
IS (mm/s)
0.44
0.40
0.36
0.32
0
20
40
60
80
100
Natural jarosite subgroup
Fe#

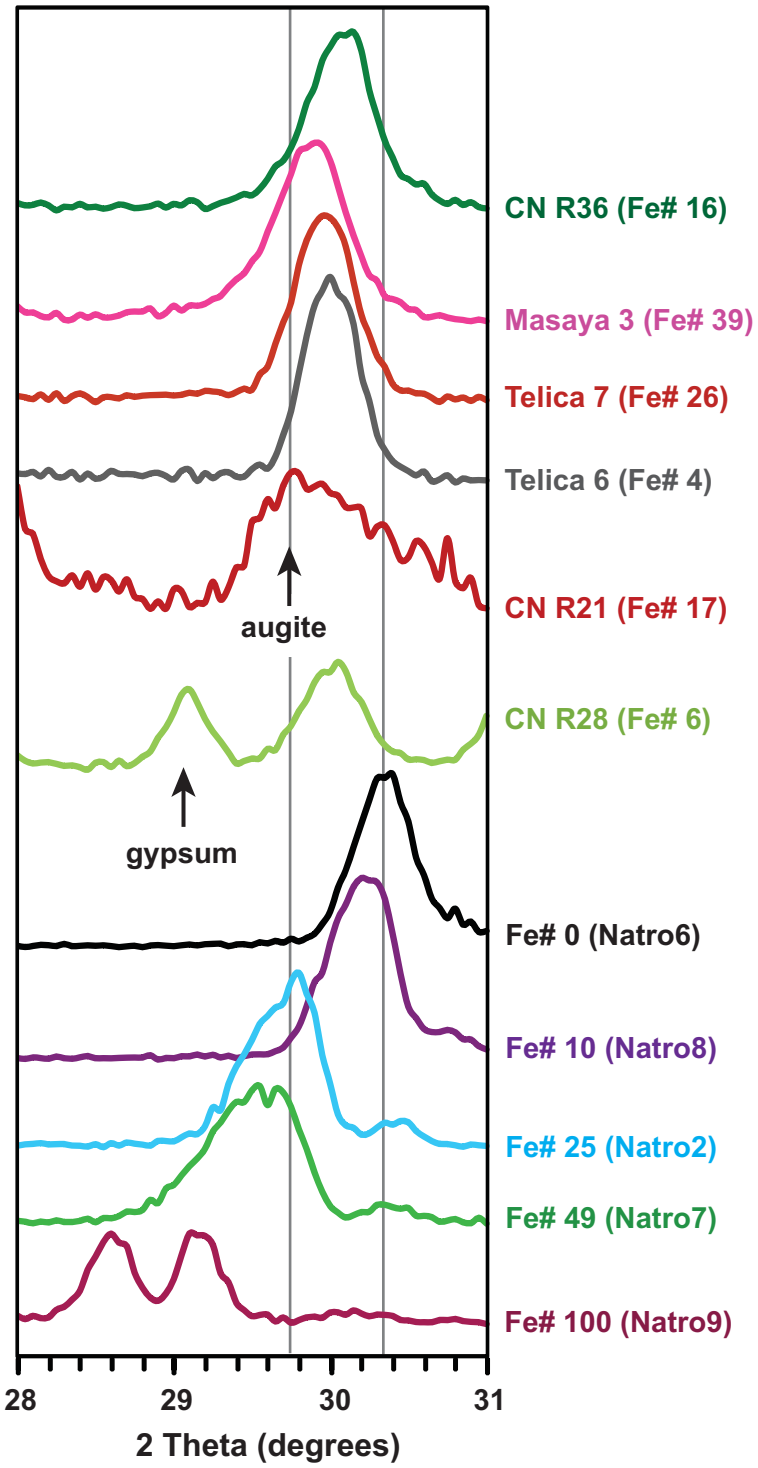
CN R36 (Fe# 16)
Masaya 3 (Fe# 39)
Telica 7 (Fe# 26)
Telica 6 (Fe# 4)
CN R21 (Fe# 17)
augite
CN R28 (Fe# 6)
gypsum
Fe# 0 (Natro6)
Fe# 10 (Natro8)
Fe# 25 (Natro2)
Fe# 49 (Natro7)
Fe# 100 (Natro9)
28
29
30
31
2 Theta (degrees)

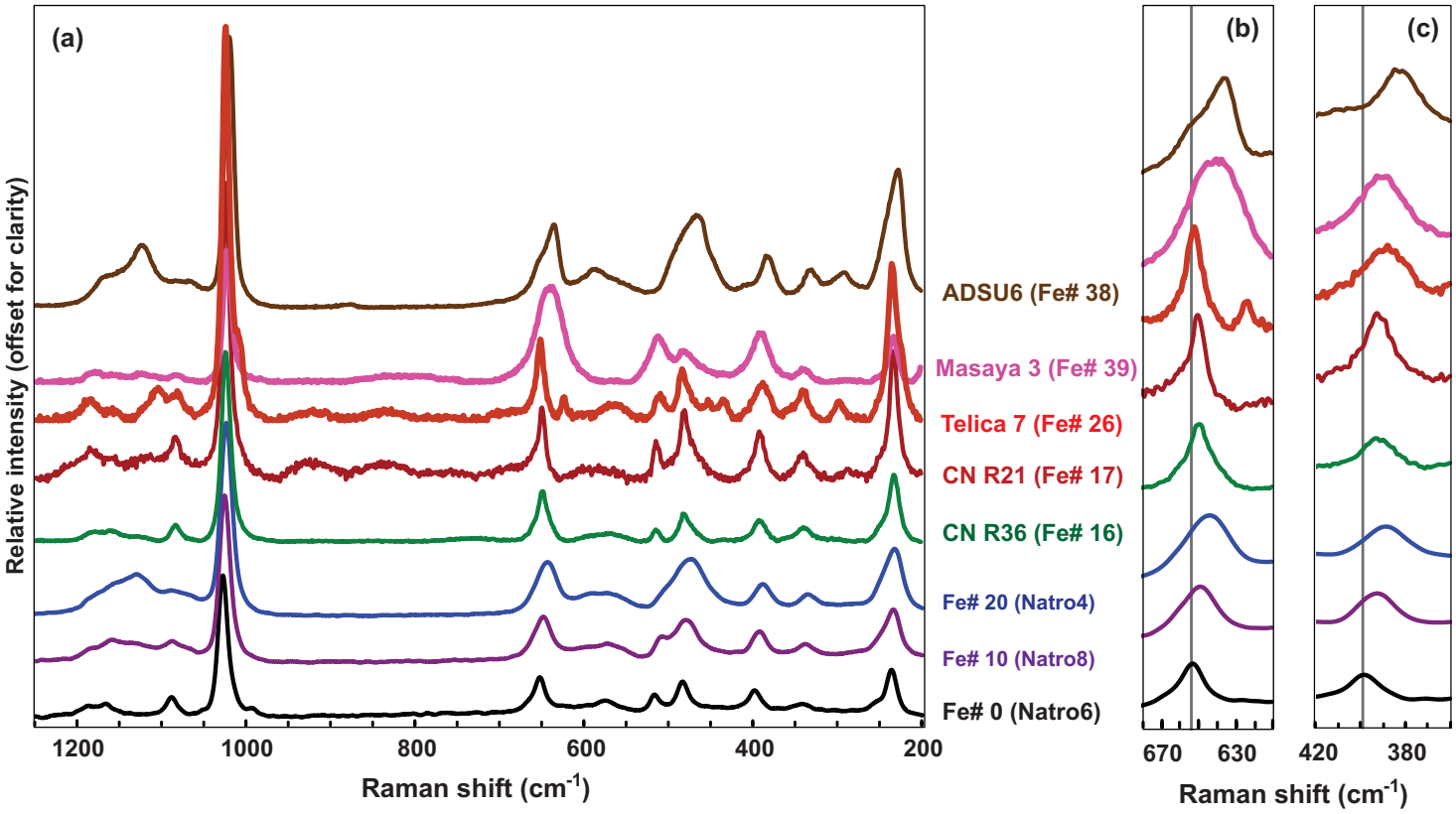
(a)
(b)
(c)
Relative intensity (offset for clarity)
ADSU6 (Fe# 38)
Masaya 3 (Fe# 39)
Telica 7 (Fe# 26)
CN R21 (Fe# 17)
CN R36 (Fe# 16)
Fe# 20 (Natro4)
Fe# 10 (Natro8)
Fe# 0 (Natro6)
1200
1000
800
600
400
200
Raman shift (cm-1)
670
630
420
380
Raman shift (cm-1)

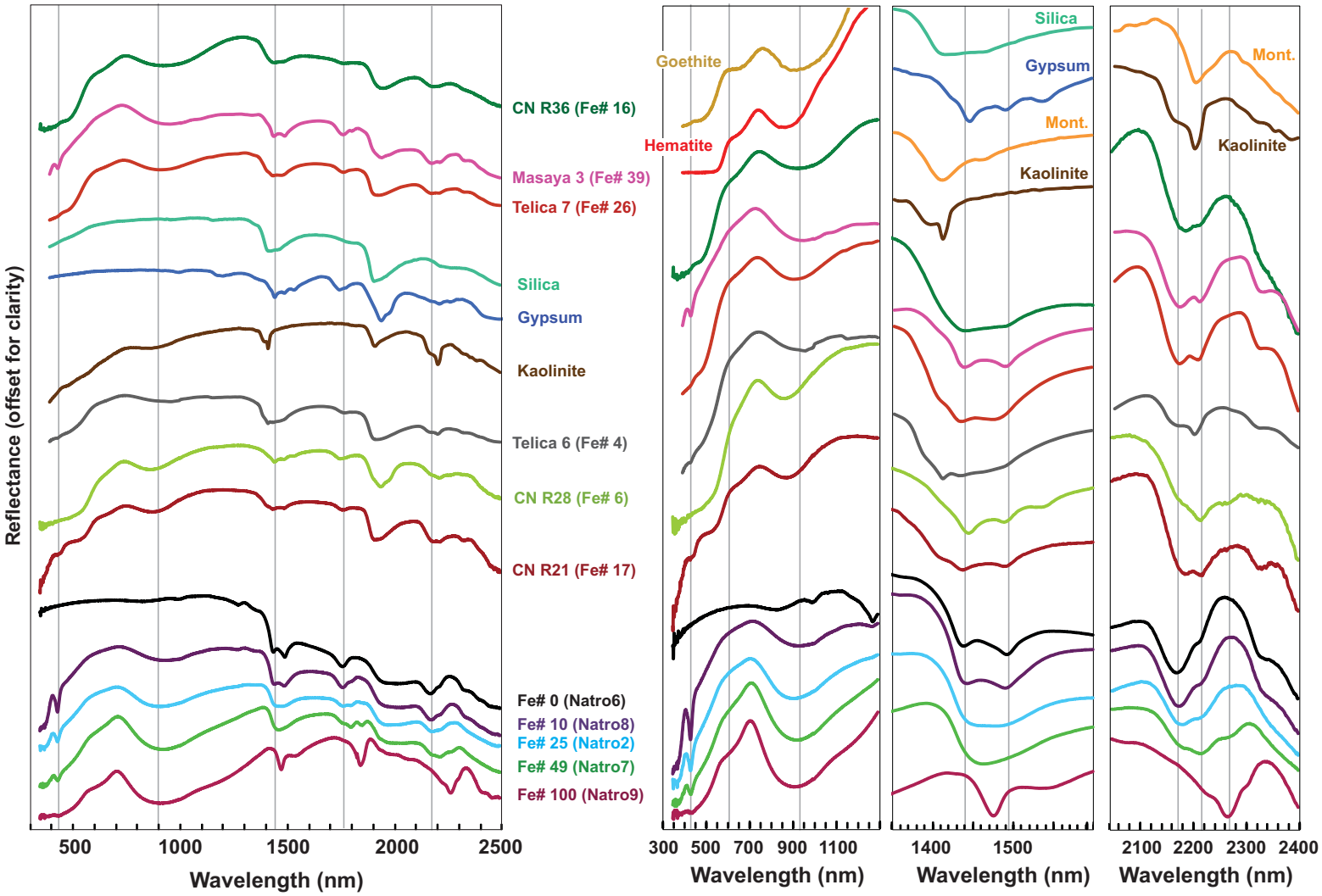
Reflectance (offset for clarity)
CN R36 (Fe# 16)
Masaya 3 (Fe# 39)
Telica 7 (Fe# 26)
Silica
Gypsum
Kaolinite
Telica 6 (Fe# 4)
CN R28 (Fe# 6)
CN R21 (Fe# 17)
Fe# 0 (Natro6)
Fe# 10 (Natro8)
Fe# 25 (Natro2)
Fe# 49 (Natro7)
Fe# 100 (Natro9)
500
1000
1500
2000
2500
Wavelength (nm)
Goethite
Hematite
300
500
700
900
1100
Wavelength (nm)
Silica
Gypsum
Mont.
Kaolinite
1400
1500
Wavelength (nm)
Mont.
Kaolinite
2100
2200
2300
2400
Wavelength (nm)

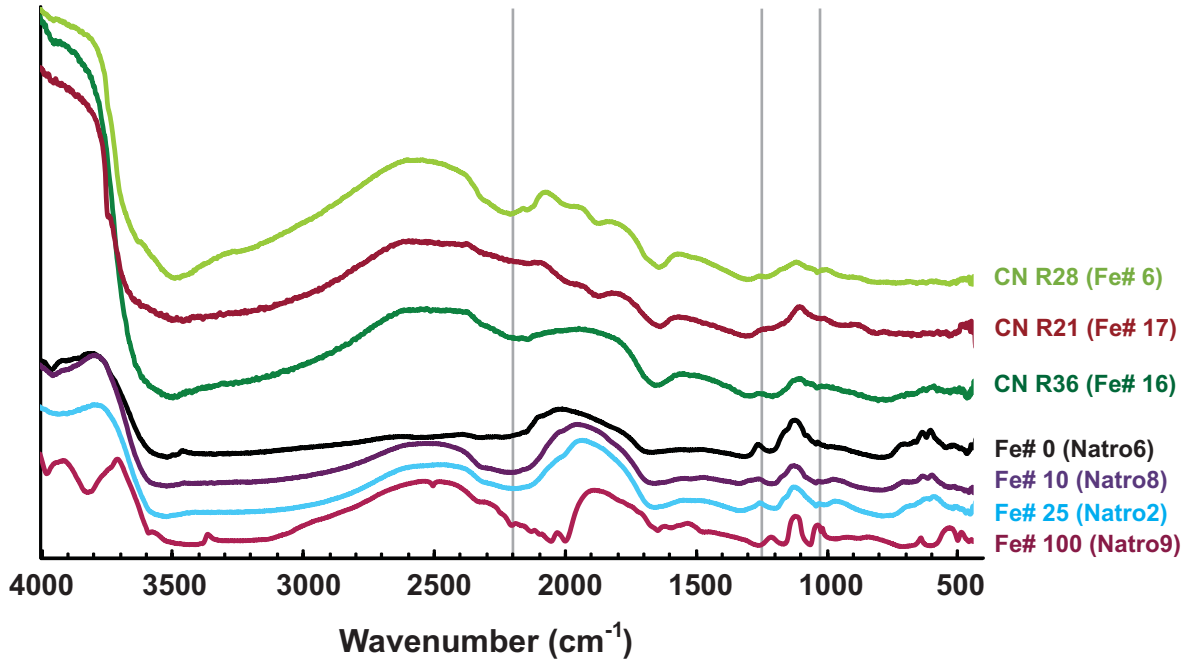
CN R28 (Fe# 6)
CN R21 (Fe# 17)
CN R36 (Fe# 16)
Fe# 0 (Natro6)
Fe# 10 (Natro8)
Fe# 25 (Natro2)
Fe# 100 (Natro9)
4000
3500
3000
2500
2000
1500
1000
500
Wavenumber (cm-1)